

# Numerical Investigation of Viscous Flow Instabilities in Multiphase Heterogeneous Porous Media

K. Christou<sup>a</sup>, W.C. Radünz<sup>a,b</sup>, B. Lashore<sup>a</sup>, F.B.S. de Oliveira<sup>c</sup>, J.L.M.A. Gomes<sup>a,\*</sup>

<sup>a</sup>*Mechanics of Fluids, Soils & Structures Group, School of Engineering, University of Aberdeen, UK*

<sup>b</sup>*Engineering School, Federal University of Rio Grande do Sul, Brazil*

<sup>c</sup>*Department of Exact and Technological Sciences, State University of Santa Cruz, Bahia, Brazil*

---

## Abstract

A critical aspect of multiphase flow in porous media is the displacement efficiency that measures the amount of fluid that can be pushed by another fluid driven by pressure gradient. Migration of contaminants and reservoir waterflooding are typical applications where understanding the dynamics of immiscible fluid displacement helps mitigating water resources contamination and improving hydrocarbons production, respectively. Due to large viscosity ratios, flow instabilities at fluids' interface may arise leading to the formation of fingers – uneven front with elongation at the outside edge of fluids interface, with strong impact on the displacement efficiency. Initial studies of viscous instabilities in Hele-Shaw cells indicated that the development of fingers mostly depends on mobility ratio and capillary number, however heterogeneity of the porous domain may also affect the onset of instabilities. Therefore, the main aim of this work is to numerically investigate formation and growth of viscous fingers in heterogeneous porous media. The model used here is based on a novel control volume finite element method (CVFEM) formulation with a family of FE-pairs,  $P_nDG-P_m$  specially tailored for Darcean flows. Dynamic mesh adaptivity enables capturing fingers development whilst saving computational overheads. Numerical experiments were performed to investigate the impact of viscosity ratio and heterogene-

---

\*Corresponding author.

Email address: jefferson.gomes@abdn.ac.uk (J.L.M.A. Gomes)

ity on Saffmann-Taylor instabilities. Numerical simulations demonstrated that the heterogeneity of the domain triggers the early-onset formation of fingers under prescribed viscosity ratio conditions. Also, effective numerical capture of growth (in particular, tip-splitting) and coalescence of dendritic finger branching induced by large viscosity ratio largely depends on mesh resolution at the fluids interface.

*Keywords:* Multi-fluid flows, Porous media, Viscous Instabilities, Mobility Ratio.

---

## 1. Introduction

Numerical investigation of multiphase flows in porous media have attracted the attention of the scientific community over the past 40 years. Characterisation of such fluid flows serves as the foundation of reservoir engineering and groundwater studies (White et al., 1981). Underground coal gasification is another important field of interest and, more recently, due to the role of green house gases (GHG) emissions in the global climate change, several research work have focused on CO<sub>2</sub> migration and trapping mechanisms in carbon capture utilisation and storage (CCUS) operations (Spycher et al., 2003; Self et al., 2012; Jiang, 2011).

Description of physics and mechanisms of multiphase porous media flows were reported by Wooding and Morel-Seytoux (1976) with focus on capillary pressure and flow regimes. A comprehensive review of force balances at the interface between immiscible fluids and resulting mechanisms for flow instabilities can be found in Homsy (1987). Flow instabilities can be classified as macroscopic and microscopic, the former is due to imposed boundary conditions, whereas the later is associated to local phenomena at the fluids interface (*e.g.*, Kelvin-Helmholtz and Saffman-Taylor instabilities, Saffman, 1959). This work focuses on flow instabilities in two-phase systems due to viscous and stress forces (often referred as viscous instabilities or viscous fingering, Section 3).

In oil and gas reservoir exploration, viscous and density instabilities are relatively common during water-injection processes. As water and oil interacts, the interface between these fluids moves creating an uneven or fingered flow profile (see Fig. 3). Viscous fingering results in inefficient flow sweeping which can bypass significant quantities of recoverable oil and may lead to

early breakthrough of water into neighbour production wells. Viscous instabilities are mainly controlled by the mobility ratio (MR) between displacing and displaced fluids. Other conditions that may also influence the severity of viscous fingering are: heterogeneity (*i.e.*, wide spatial porosity and/or permeability distribution), gravitational forces, anisotropic dispersion, non-monotonic viscosity profile etc (Budek et al., 2017; Nicolaides et al., 2015).

Multi-fluid flow dynamics in porous media are described by continuity and momentum (extended Darcy's law) conservative equations for each fluid (or phases) with coupling mass terms (*i.e.*, density and saturation) appearing in both sets of equations. Advanced numerical methods are in continuous development to accurately represent force balances in Darcian flows. Finite difference methods (FDM) have been extensively used in most industry-standard reservoir simulators (Aziz and Settari, 1986; Chen et al., 2005; Chang et al., 1990) with relative success. However, they are often limited to relatively simple geometries representing idealised geological formations through structured quadrilateral (2-D) and hexahedral (3-D) grid cells (Mlacnik et al., 2004; King and Mansfield, 1999). Additionally, FDM schemes often result in excessive numerical dispersion when strong heterogeneity (represented by permeability and porosity fields) is present (Chavent and Jaffré, 1986).

The geometrical flexibility associated with high-order numerical accuracy of finite element methods (FEM) has proven to be more efficient than FDM to solve fluid flow dynamics in complex geometries. Among FEM-based formulations for porous media, the control volume finite element methods (CVFEM, Fung et al., 1992) has been widely used as it can guarantee local mass conservation and high-order numerical accuracy as well as being able to use tetrahedral geometry-conforming elements. In traditional CVFEM formulations, pressure and velocity are interpolated using piecewise linear FE basis functions, while material properties and flow conditions (*e.g.*, phase saturation, density, temperature, species concentration etc) are represented with CV basis functions (Voller, 2009). Saturation equations are solved explicitly after solving for the dual pressure-velocity at each non-linear iteration (a detailed description of the implicit pressure explicit saturation, IMPES, formulation can be found in Chen et al., 2006; Lux and Anguy, 2012).

Since geometries are captured by finite elements, constructed control volumes typically extend on each side of the interface which may have different properties. Therefore, some average values of the coupled velocity-pressure

fields (defined in the FE space but projected onto the CV space) are applied across the CVs at these interfaces. These often lead to excessive numerical dispersion especially in highly heterogeneous media (represented by spatial-dependent permeability and porosity fields). In order to overcome such artificial numerical dispersion, a discontinuous hybrid finite element finite volume method (DFEFVM) formulation was introduced by [Nick and Matthai \(2011a,b\)](#). This novel discretisation scheme was designed to simulate flows through discrete fractured rocks in which CVs are divided along the interfaces of different materials. [Cumming et al. \(2011\)](#) demonstrated that CVFEM discretisation could also be used to solve Richards' equations (coupled mass conservation and Darcy equation) in heterogeneous media with relatively small computational overhead (compared with traditional coupled velocity-pressure based formulations, see also [Cumming, 2012](#)). Fluxes over CVs were calculated based upon material properties, whereas the saturation field was volume-averaged at the interface of the materials, enforcing mass balance as described by [Kirkland et al. \(1992\)](#).

In this work, a novel CVFEM formulation, previously introduced by [Gomes et al. \(2017\)](#) (see also [Jackson et al., 2015; Salinas et al., 2015](#)), is used to numerically investigate formation and growth of viscous fingers in heterogeneous porous media. The continuity equation is embedded into the pressure equation to enforce mass conservation whilst ensuring that the force balance is preserved. A hybrid family of  $P_n$ DG- $P_m$  triangular and tetrahedral FE pairs is used to discretise velocity and pressure. A sketch of the  $P_1$ DG- $P_2$  FE-pair is shown in Fig. 1, in which velocity is represented by discontinuous and piecewise linear basis functions whereas pressure is interpolated through continuous and piecewise quadratic basis functions. Scalar fields are stored in CV space (Fig. 2). The dual pressure and velocity fields are represented simultaneously (through non-linear projections) in FE and CV spaces.

A brief description of the numerical formulation and viscous fluid instabilities are introduced in Sections 2 and 3, respectively. Model set up and results including initial model-benchmark are presented in Section 4. Impact of mobility ratio on the fingers formation is also included in this section. Finally, concluding remarks are presented in Section 5.

## 2. Model Formulation

The two-phase immiscible and incompressible fluid flow through a porous media domain  $\Omega$ , may be described by the coupled extended Darcy and

saturation equations,

$$\left( \frac{\mu_\alpha S_\alpha}{\mathbf{K} \mathcal{K}_{r,\alpha}} \right) \mathbf{u}_\alpha = \underline{\sigma}_\alpha \mathbf{u}_\alpha = -\nabla p + \mathcal{S}_{u,\alpha} \quad \text{with } x_i \in \Omega, t > 0, \quad (1)$$

$$\phi \frac{\partial S_\alpha}{\partial t} + \nabla \cdot (\mathbf{u}_\alpha S_\alpha) = \mathcal{S}_{cty,\alpha} \quad \text{with } x_i \in \Omega, t > 0, \quad (2)$$

respectively, where  $\mu$ ,  $\mathbf{K}$ ,  $p$  and  $\phi$  are viscosity, absolute permeability, pressure and porosity, respectively.  $\mathbf{u}_\alpha$  is the saturation-weighted Darcy velocity of the  $\alpha$ -phase and  $\mathcal{K}_{r,\alpha}$  is the relative permeability.  $\mathcal{S}$  is the source term associated with the Darcy and continuity equations.  $S_\alpha$  represents the saturation of the  $\alpha$ -phase with mass conservation constraints of  $\sum_{\alpha=1}^{\mathcal{N}_p} S_\alpha = 1$ , where  $\mathcal{N}_p$  denotes the number of phases.  $\underline{\sigma}_\alpha$  is an absorption-like term that represents the implicit linearisation of the viscous frictional forces.

The formulation introduced here is applicable to  $\mathcal{N}_p$  fluid phases and is based on two families of FE-pairs:  $P_n$ DG- $P_m$ DG and  $P_n$ DG- $P_m$  ([Cotter et al., 2009](#)), consistent with the dual pressure-velocity representation in CV space. In these families of FE-pairs, velocity is represented by  $n^{\text{th}}$ -order polynomials that are discontinuous across elements, whereas pressure is represented by  $m^{\text{th}}$ -order polynomials that may be either continuous or discontinuous (thus the notation  $P_n$ DG- $P_m$  and  $P_n$ DG- $P_m$ DG, respectively) across elements. Mass balance (continuity) equations are solved in CV space and a Petrov-Galerkin FEM is used to obtain high-order fluxes on CV boundaries, which are limited to yield bounded fields (*e.g.*, positive densities, saturations bounded between 0 and 1, etc). Simulations performed for this work were conducted using two types of elements:  $P_1$ DG- $P_1$  and  $P_1$ DG- $P_2$ .

Finite element basis functions for velocity and pressure fields are introduced in the discretisation of force-balance equations. Hybrid basis functions are also used to allow CV-based velocity to be extrapolated across the entire element. The extended Darcy equation (Eqn. 1) is discretised using a FE representation of  $\mathbf{v}_\alpha = \underline{\sigma}_\alpha \mathbf{u}_\alpha$  and  $p$  with FE basis functions  $Q_j$  and  $P_j$ , respectively – note that  $\underline{\sigma}_\alpha$  lies in both CV and FEM spaces. Each component of the weak form of the extended Darcy equation is tested with the  $\mathbf{v}_\alpha$  basis

function,  $Q_j$ , to obtain:

$$\sum_E \int_{\Omega_E} Q_i (\mathbf{v}_\alpha + \nabla p - \mathbf{s}_{u_\alpha}) dV + \oint_{\Gamma_E} Q_i \mathbf{n} (p - \tilde{p}) d\Gamma + \oint_{\Gamma_\Omega} Q_i \mathbf{n} (p - p_{bc}) d\Gamma = \mathbf{0}, \quad (3)$$

where  $\Omega_E$  and  $\Gamma_E$  are the volume and boundary of element  $E$ , respectively, and  $\Gamma_\Omega$  is the boundary of the computational domain. The numerical pressure  $\tilde{p}$  appearing in the jump condition (second term in Eqn. 3) is the arithmetic mean of the potentially discontinuous pressure across the element  $E$  (consistent with the  $P_n$ DG- $P_m$ DG element-pairs). This term vanishes when a continuous formulation is used to discretise the pressure field (with  $P_n$ DG- $P_m$  element-pairs). The last term in Eqn. 3 is used to weakly enforce the pressure level to  $p_{bc}$  on a computational domain boundary.

Whilst saturation (and all saturation-dependent material properties such as relative permeability and capillary pressure) is calculated in CV space, absolute permeability is assumed piecewise constant in FE space. Saturation equations (Eqn. 2) are discretised in space with CV basis function,  $M_i$ , and with the  $\theta$ -method in time (Gomes et al., 2012). Velocities across CV interfaces (within and between elements) are calculated through a directional-weighted flux-limited scheme based on upwind value of  $\sigma$  at individual CV as described by Jackson et al. (2013). Summing the discretised Eqn. 2 over all phases yields the global mass balance equation,

$$\sum_{\alpha=1}^{N_p} \left\{ \int_{\Omega_{CVi}} M_i \frac{\phi (S_{\alpha i}^{n+1} - S_{\alpha i}^n)}{\Delta t} dV + \oint_{\Gamma_{CVi}} [\theta^{n+1/2} \mathbf{n} \cdot \mathbf{u}_\alpha^{n+1} S_\alpha^{n+1} + (1 - \theta^{n+1/2}) \mathbf{u}_\alpha^n S_\alpha^n] d\Gamma - \int_{\Omega_{CVi}} M_i \mathcal{S}_{cty,\alpha}^{n+\theta} dV \right\} = 0, \quad (4)$$

where  $\Omega_{CVi}$  and  $\Gamma_{CVi}$  are the volume and boundary of CV  $i$  respectively,  $M_i$  are CV basis functions,  $\mathbf{n}$  is the outward pointing unit normal vector to the surface of  $CV_i$  and  $n$  is the current time level.  $\theta$  varies smoothly between 0.5 (corresponding to Crank-Nicolson method) and 1 (corresponding

to backward-Euler scheme) to avoid the introduction of spurious oscillations for large grid Courant numbers.

The discretised global mass and force balance equations are solved using a multigrid-like approach as described by Pavlidis et al. (2016) (see also Salinas et al., 2016). The numerical formulation is fully described by Gomes et al. (2017) (see also Salinas et al., 2015; Adam et al., 2016).

### 3. Brief Summary of Viscous Instabilities

The study of viscous flow instabilities (*i.e.*, fingering) is particularly important in oil exploration due to heterogeneities (*i.e.*, natural fractures, permeability and/or porosity characteristics in different zones) of geological formations. A major problem associated with water-flooding processes is the early water-breakthrough caused by high-permeability layers and unfavorable mobility ratios. Water breakthrough and volumetric sweep efficiency (ratio of volumes between the recovered and the injected fluids) are the main determinants of the productive life of a reservoir (Riaz and Tchelepi, 2004; Tavassoli et al., 2015). During immiscible CO<sub>2</sub>-flooding (*i.e.*, in CO<sub>2</sub> enhanced oil recovery, CO<sub>2</sub>-EOR, processes), viscosity of supercritical CO<sub>2</sub> is lower than crude oil, thus viscous fingering and/or channelling may occur.

The efficiency of fluid displacement depends upon the ratio of viscous and capillary forces (or capillary number,  $N_c$ , Eqn. 5). When viscous force of the injected fluid overcomes the capillary force, hydrodynamic instabilities may occur, resulting in the collapse of the interface between fluids and fingers start to form.

Viscous flow instabilities can be found across several disciplines and scales, from chemical separation processes to geological reservoir fluids. Muskat (1934) investigated fluid flow in Hele-Shaw cells, *i.e.*, parallel flat plates separated by an infinitesimal gap, and the impact on the capillary number ( $N_c$ ),

$$N_c = \frac{\mu U}{\gamma}. \quad (5)$$

In Eqn. 5,  $\gamma$  is the surface tension and  $U$  is the characteristic velocity of the moving interface. This experimental apparatus enables instabilities to be qualitatively investigated by simplifying the flow in both porous and non-porous media into a 2D problem.

More recently, [Howison \(2000\)](#) and [Praud and Swinney \(2005\)](#) provided a comprehensive description of the mathematical formulation of immiscible two-phase flows in Hele-Shaw cells (also known as Saffman & Taylor problem). For a Hele-Shaw cell of a given size, flow development depends only on the capillary number. Thus if  $N_c$  is too high, [Saffman \(1959\)](#), [Homsy \(1987\)](#) and [Tabeling et al. \(1987\)](#) determined that the flow develops into a single steady-state finger which moves through the cell with constant velocity  $U$ .

Under the assumption that fluids remain immiscible along an interface, surface tension plays an important role in determining the shape and progress of the fingers ([Howison, 2000](#)). During the displacement of a fluid by a less viscous one, the expected uniform front ([Buckley and Leverett, 1942](#); [Sheldon and Cardwell, 1959](#)) is perturbed leading to an uneven front with elongations at the outside edge of the fluid interface (Fig. 3), often referred as *fingers*. In homogeneous domains, fingers start to develop when the surface tension acting on the interface between the fluids exert an opposite force towards the change of shape of the interface. The interface becomes unstable and collapses, taking a curved shape ([Homsy, 1987](#); [Jackson et al., 2017](#)).

In heterogeneous domains, such instability may be triggered by permeability differences across regions as demonstrated in Section 4.3. The higher the velocity of the low viscosity fluid, the less wide (tip-splitting behaviour) the finger is. Pressure differences acting on the interface produces a net pressure force,

$$\Delta P = -\gamma \nabla \cdot \hat{n}. \quad (6)$$

This expression is also known as the Young-Laplace equation, a relation describing the capillary pressure across the interface between two fluids, with  $\Delta P$  denoting the pressure difference and  $\hat{n}$  is the unit normal vector out of the surface.

As demonstrated by [Habermann \(1960\)](#) (see also [Budek et al., 2017](#)), mobility ratio (MR) is a key-parameter to assess fluid displacement and is defined as the ratio of mobility of the displacing (fluid  $i$ ) to that of the displaced fluid ( $j$ ),

$$MR = \frac{\mathcal{K}_{ri}\mu_j}{\mathcal{K}_{rj}\mu_i}. \quad (7)$$

MR is a function not only of fluids' viscosity and saturation, but also of the parameterised relative permeability,  $\mathcal{K}_{r\alpha}$ , which is often expressed as a function of local, residual and maximum phase saturations prescribed in the

pore rock matrix. In the simulations conducted for this work, the modified [Brooks and Corey \(1964\)](#) model was used ([Alpak et al., 1999](#)),

$$\mathcal{K}_{rw}(S_w) = \mathcal{K}_{rw}^{\circ} \left[ \frac{S_w - S_{w,irr}}{1 - S_{w,irr} - S_{nw,r}} \right]^{n_w}, \quad (8)$$

$$\mathcal{K}_{rnw}(S_{nw}) = \mathcal{K}_{rnw}^{\circ} \left[ \frac{S_{nw} - S_{nw,r}}{1 - S_{w,irr} - S_{nw,r}} \right]^{n_{nw}}, \quad (9)$$

where subscripts  $w$  and  $nw$  stand for wetting and non-wetting phases, respectively.  $\mathcal{K}_{rw}^{\circ}$  and  $\mathcal{K}_{rnw}^{\circ}$  are end-point relative permeability to wetting and non-wetting phases,  $S_{w,irr}$  and  $S_{nw,r}$  are irreducible wetting and residual non-wetting phase saturations, respectively. Exponents  $n_w$  and  $n_{nw}$  are both set to 2.

From Eqns. 7-9, it is clear that during fluid displacement, the mobility ratio changes as phase saturation,  $S_w(x_i, t)$  and  $S_{nw}(x_i, t)$ , varies in time and space (Eqn. 2). Therefore, with no lack of generality, the MR can be reduced to the viscosity ratio (VR),

$$VR = \frac{\mu_i}{\mu_j},$$

that will be used in the parametrisation of the numerical simulations conducted in Section 4. Analysis performed in the following sections will make use of this simplified definition as phase saturation ( $S_\alpha$ ) is a time- and spatial-dependent prognostic field which is calculated along with pressure ( $p$ ) and velocity ( $\mathbf{u}_\alpha$ ) fields.

In immiscible displacements, viscous fingering occurs when the viscosity ratio is greater than unity. As surface tension becomes weak, the interface is stressed and becomes unstable leading to the formation of fingers. At this point it should be mentioned that there are two parameters – Peclet number (Pe) and mobility ratio (MR), that determine the flow stability characteristics. There are always a few dominant fingers that spread and shield the growth of other fingers. The interface of the main finger collapses and starts splitting into new lobes of fingers. One of these new fingers may eventually outgrow the others and then spreads to occupy an increasingly larger width. In the process, the finger reaches a critical width while the saturation of its front becomes steep as a result of stretching caused by the cross-flow, causing the tip of the finger to become unstable and splits again, and the pattern repeats itself. Therefore, surface tension plays an essential dual role,

it must be weak enough for the tip front to be unstable, but it is also the physical force causing the spreading and ensuing repeated branching (Tan and Homsy, 1988; Carvalho et al., 2013).

In the next section, the numerical formulation used to simulate multi-fluid flow in porous media is briefly validated (Section 4.2) against laboratory experiments (qualitative validation). The impact of VR (quantitative validation) and heterogeneity on the onset instability and growth of fingers are numerically investigated in Section 4.3. Section 4.4 demonstrates the importance of an appropriate mesh resolution to adequately capture the initial stages of viscous fingers formation and development. Finally, flow pathway (channelling) is the focus of Section 4.5.

## 4. Results

### 4.1. Model Set-up

Numerical simulations were conducted with the model summarised in Section 2 and embedded in the next-generation flow simulator Fluidity/IC-FERST model software<sup>1</sup> (a full description of the model can be found in Jackson et al., 2013; Gomes et al., 2017). This multi-physics model has been validated against traditional multi-fluids test-cases (*e.g.*, advection-diffusion, Buckley-Leverett problem, channel model, immiscible displacement, gravity-driven displacement etc) in Radünz et al. (2014), Jackson et al. (2015), Salinas et al. (2015) and Pavlidis et al. (2016).

In this work, all test-cases were performed in idealised geometries discretised with unstructured triangular and tetrahedral mesh using the P<sub>1</sub>DG-P<sub>2</sub> and P<sub>1</sub>DG-P<sub>1</sub> FE-pairs (Fig. 2). An implicit Crank-Nicolson time-stepping scheme was used with *a posteriori* adaptive time-step size targeting a maximum Courant-Friedrichs-Lowy condition (CFL, Courant et al., 1941) of 2. In most simulations, the domain was initially fully saturated with non-wetting fluid which was displaced by a pure (wetting) fluid at a prescribed initial velocity ( $u^0$ ). For simplicity, the porosity ( $\phi$ ) of the domain was kept constant at 0.2 in all simulations, whereas the absolute permeability ( $\mathbf{K}$ ) varied in space, *i.e.*,  $\mathbf{K} = \mathbf{K}(x_i)$ . Fluids are assumed incompressible and gravity was neglected. Initial set-up for the numerical simulations is summarised in Table 1.

---

<sup>1</sup><http://multifluids.github.io>

#### 4.2. Initial Model Validation

Numerical simulations (based on lab experiments due to [Evans and Dawe, 1994](#); [Dawe and Grattoni, 2008](#)) were conducted to demonstrate the model capability to capture viscous crossflow during immiscible displacement in heterogeneous porous media. The 2D domain, shown in Fig. 4, is  $4 \times 2$  unit-length and fully saturated with fluid 2 ( $VR=1$ ). Fluid 1 is injected from the left-hand side of the domain with constant velocity of  $u = 1$ . Boundary conditions also include no-flux across upper and lower borders. The domain consists of four regions in which each quarter is represented by a permeability value, Fig. 4(a). The spatial permeability distribution creates a rough pressure field, *i.e.*, pressure gradient is discontinuous across the interface between different permeability zones, thus the fluid flows to the larger permeability region.

A two-phase immiscible flow along homogeneous and parallel layers of contrasting petrophysical properties (*i.e.*, permeability) is initially simulated. During the fluid displacement, crossflow between adjacent layers often occur due to viscous, capillary and/or gravitational forces that drive the flow. In this numerical simulation, crossflow is caused by viscous forces, which is commonly named viscous crossflow. Figures 4(b) and (c) show the continuous displacement of fluid 2 due to the injection of fluid 1. They also demonstrate the preferential flow path through high-permeability regions. Such flow behaviour, represented by the crossflow through the four regions, is in good qualitative agreement with experiments conducted by [Dawe and Grattoni \(2008\)](#).

#### 4.3. Flow Simulations in Hele-Shaw Cells at Different Viscosity Ratio Conditions

In order to investigate the impact of viscosity ratio on the flow dynamics, numerical simulations of fluid displacement were conducted in Hele-shaw cells following the work of [Saffman \(1986\)](#). In this manuscript, the onset of viscous flow instabilities (following his seminal work in [Saffman and Taylor, 1958](#)) is investigated along with the impact of boundary conditions in the problem's mathematical formulation and solutions.

Here, 2D simulations were conducted in a  $5 \times 5$  cm domain (Fig. 5a) fully saturated with a fluid. Wetting phase fluid is driven from the bottom left-hand corner of the domain with velocity of  $1 \text{ cm.s}^{-1}$  (magnitude). No-flux boundary conditions were imposed to all borders of the domain except at the

top right-hand side corner (named as sink), and a pressure gradient between source and sink regions was initially imposed to the system.

Figures 5-7 show fluid displacement in simulations conducted with  $VR = \{3, 10, 150\}$ , respectively. At relatively low viscosity ratio conditions (*i.e.*,  $VR=3$ ), saturation evolves in time with a smooth front throughout most of the domain, and no finger could be observed. Elongated saturation profile at later stages of the simulation is due to pressure gradient near the sink region. However, formation of fingers can be readily noticed at early stages of simulations conducted with viscosity ratios of 10 and 150.

Viscous finger morphologies were investigated by [Guan and Pitchumani \(2003\)](#) based on mathematical formulation and semi-analytic solutions of the coupled Darcy and continuity equations developed by [McLean and Saffman \(1981\)](#). They conducted a sensitivity analysis to investigate fingers' formation, dimensions and branchiness for a range of viscosity ratios ( $10^2 \leq VR \leq 10^4$ ) and modified capillary numbers ( $632 \leq N'_C \leq 6.32 \times 10^7$ , with  $N'_C = U_f \mu \gamma^{-1} (W/b)^2$ , where  $U_f$  is the velocity of the finger,  $W$  is half Hele-Shaw cell width and  $b$  is the cell thickness). Finger width ( $\lambda_f$ ) and volumetric flow rate ( $\mathcal{Q}$ ) at the outflow region are correlated through,

$$\mathcal{Q} = U_f b \lambda_f. \quad (10)$$

Here, numerical simulations performed with viscosity ratio of 10 and 150 indicated maximum fingers width of approximately 0.45-0.70 and 0.50-0.90 cm (Fig. 8 a and b), respectively. This is in close agreement with expected values obtained from Eqn. 10 which indicates maximum finger width ranging from 0.13 to 0.75 (for  $VR=10$ ) and from 0.30 to 0.75 ( $VR=150$ , Table 2).

Fluid flow dynamics through heterogeneous porous media are sensibly more complex than in homogeneous media and strongly depend on problem properties. Studies by [Langtangen et al. \(1992\)](#) on fluid flow dynamics in heterogeneous porous media (analytical and numerical solutions) demonstrated that hyperbolic Buckley-Leverett model is inherently unstable, *i.e.*, the expected uniform interface front collapses as any perturbation in physical parameters are imposed to the problem.

Spatial variation in geological formations occurs in all length-scales, where heterogeneity characteristics in small length-scales (*i.e.*, pore) are statistically embedded into permeability (absolute and relative) and porosity parameters. Such multi-scale heterogeneity induces preferential flow pathways

and plays a significant role in the onset of fluid instabilities as it triggers fingers formation and their accelerated growth (see Wing et al., 1989; Tchelepi and Jr, 1994).

In order to qualitatively investigate the impact of heterogeneity (here represented by changing in the permeability field), numerical simulations were conducted using a prescribed permeability distribution and viscosity ratios of 10 and 150. Absolute permeability ranging from  $1.0 \times 10^{-12}$  to  $5.0 \times 10^{-10}$  cm<sup>2</sup> (*i.e.*,  $0.1 \leq K \leq 50$  milidarcy) was used in the simulations, which were performed with the same geometry, mesh resolution, boundary and initial conditions as in previous homogeneous cases(Figs. 5-8b).

Figures 9 and 10 show formation of multi-scale elongations with continuous growth and coalescence of dendritic finger branching in simulations performed with viscosity ratio of 10 and 150, respectively. In both simulations, maximum fingers width of approximately 0.44-0.56 ( $VR=10$ ) and 0.24-0.44 cm were found, whereas estimated values (based on Eqn. 10) were 0.25-4.50 ( $VR=10$ ) and 0.88-3.00 cm ( $VR=150$ ) – Fig. 8 c-d, Table 2. Such calculated ranges (*i.e.*, theoretical values based on analytic solutions due to McLean and Saffman, 1981) clearly overestimate fingers dimensions as the mathematical formulation (and therefore Eqn. 10) assumes incompressible flows in homogeneous porous medium, *i.e.*, it does not take into account any spatial variability of heterogeneity.

#### 4.4. Capturing Flow Dynamics and Fingering Growth: Impact of Mesh Resolution

In most numerical simulations involving geo-fluid dynamics, local geometric constraints (*e.g.*, faults, fractures etc) and spatial multi-scale variability of flow properties are often ignored as the underlying computational mesh grid is too coarse to reliably represent any of these features. Whilst structured grids often struggle to conform to complex domain boundaries with consistent mesh connectivity, unstructured mesh techniques often relax cells' neighbourhood relationship constraints by dividing the domain into polytopes in which elements share adjacent faces. This leads to mesh grids that conform to the domain topography and can make the best use of state-of-the-art self-adaptive computational methods.

In Section 4.3, the impact of viscosity ratio on the growth of fingers and the triggering effect of heterogeneity on instability's nucleation were demonstrated in modified simulated Hele-Shaw cells. In order to capture the

continuous development of viscous instabilities, mesh grids with sufficient resolution need to be applied over the interface between fluids. Figure 11 shows a numerical simulation performed with the same geometry, boundary and initial conditions as the one shown in Fig. 10, but with noticeable lower resolution (3734 instead of 26313 elements). As it can be seen, the lower the resolution the more difficult is to capture the fingers formations, growth and branching.

Traditional computational geo-fluid dynamics (CGFD) models often rely on fixed mesh with sufficient resolution throughout the domain to capture specific flow dynamics (*e.g.*, fluid instabilities, flow re-circulation, heat and mass transfers etc), however computational overhead may be prohibitive for simulations involving complex geometries and heterogeneous properties. Mesh adaptivity methods have been extensively used by the CGFD community to help capturing detailed flow dynamics, compositional non-equilibrium fluid displacement and solid-fluid interactions (Paluszny et al., 2007; Pietro et al., 2014; Su et al., 2016; Melnikova et al., 2016). In these methods, the mesh grid is continuously modified (*i.e.*, adjustments of the number and distribution of the degrees of freedom to reduce solution error) to focus resolution where is necessary as the simulation evolves in time and space. There are four main families of mesh adaptivity methods: adaptive mesh refinement (AMR), edge and face element manipulations whereas keeping the order of the element basis function fixed (h-adaptivity), mesh deformation (r-adaptivity) and changes of element basis function order (p-adaptivity). Detailed description and analysis of mesh adaptivity methods are beyond the scope of this manuscript but can be readily found in Lo (2015) (see also Plewa et al., 2004; Frey and George, 2008).

The dynamic mesh adaptive algorithm embedded in the Fluidity/IC-FERST model utilises a metric tensor field dependent on solution interpolation error-estimates which locally control the topology of elements in the metric (Pain et al., 2001; Power et al., 2006). Mesh optimisation generates unstructured finer mesh in regions where flow properties change faster, and coarser mesh in regions where properties change more slowly (Piggott et al., 2006). The mesh adapts in three stages: metric formation, mesh optimisation and fields' interpolation from the pre- to post-adapted mesh (see Hiester et al., 2014). In the simulations shown in this work, mesh will adapt as a response to oscillations in the phase saturation field with prescribed interpolation error estimate (Mostaghimi et al., 2016).

Here, two numerical simulations were conducted with fixed and adaptive mesh resolutions to qualitatively assess model capability to capture fingers dynamics. In order to trigger the formation of fingers, regions with sharp permeability gradient were introduced. The computational domain, Fig. 12a, consists of a rectangular geometry fully saturated with a fluid (except by a squared region containing 50% of a second fluid – wetting fluid phase, Fig. 12b) and divided into 5 regions with prescribed permeability distribution. A no-flux boundary condition was imposed across upper and lower borders, whilst pure wetting fluid phase (*i.e.*,  $S_1 = 1$ ) is driven into the domain from the left-hand side face at velocity  $u_1 = 1$ . Viscosity ratio was set to 10.

Figures 13 and 14 show fluid displacement in simulations performed with fixed and adaptive meshes. Both simulations started with a mesh of 13068 triangular ( $P_1$ DG- $P_2$ ) elements, however as flow dynamics evolve the number of elements of the simulation conducted with adaptive mesh oscillates from a minimum of 4400 to a maximum of 16430 (Fig. 15). In both cases, fingers' development (formation, growth and coalescence) and fluid cross flows (through regions of distinct permeabilities at the top of the domain,  $\mathbf{K} = \{2, 3\}$ ) can be readily noticed. The simulation performed with a fixed and relatively fine mesh was able to capture the progressive development of fingers (as shown in Fig. 16b) prompted by sharp permeability gradient at the interface of regions with  $\mathbf{K} = \{1, 5\}$ . In regions with no permeability gradient, formation and development of fingers (Fig. 16c) were not captured by the simulation conducted with fixed mesh. In both cases, dynamic adaptive mesh based on perturbation of phase saturations with imposed interpolation error estimate proved to be able to capture the onset of instabilities and fingers' development with relatively little computational overhead, as indicated in Fig. 15.

#### 4.5. 3-D channel flows

In geological formations, preferential pathways flows may result in fast pollutant transport (advection-diffusion-dispersion) after industrial spillage (therefore leading to contamination of groundwater) or low hydrocarbon recovery rates (in water-,  $CO_2$ - and/or polymer-flooding operations in oil/gas field exploration). In this Section, 3D simulations are conducted to investigate preferential flow pathways through semi-pervious and impervious geological layers.

The computational domain with permeability distribution of  $10^{-4} \leq \mathbf{K} \leq 10^5$  miliarcy (Fig. 17) was designed to naturally capture preferential

flow pathways through channels of large absolute permeability. Pure (wetting) fluid is added into the domain with uniform velocity of  $2.5 \text{ cm.s}^{-1}$  from the left-hand side face. No-flux boundary conditions are applied to all borders, except at the inlet (left-hand side) and outflow (right-hand side) faces. Initially, the domain was partially saturated with non-wetting fluid, *i.e.*,  $S_{nw}(t = 0) = 0.80$ , which was continuously displaced by the wetting fluid as the simulation progress. The domain was discretised with 235k tetrahedral P<sub>1</sub>DG-P<sub>1</sub>DG element-pairs.

As demonstrated in the preliminary model validation (Section 4.2), cross-flow towards the upper region of the initial part of the domain is due to boundary pressures and diffusivities (both at different vertical layers), *i.e.*, caused by large permeability gradients (Fig. 18). As the simulation progresses, non-wetting fluid is driven from regions with lower fluid resistance (central channel), although adjacent region (with low permeability) remains stagnant.

Such preferential flow pathways are clearly indicated in Fig. 19, where Darcy velocity vectors overlapped with wetting phase fluid saturation are shown. Fluid displacement occurs mainly in regions of relatively larger permeability, leaving other parts of the domain (*i.e.*, regions with low permeability distribution) with little or no momentum, indicating that at these regions the non-wetting fluid (*i.e.*, fluid 2) is not effectively displaced.

In Sections 4.3-4.4, finger's formation, growth and branching were triggered by domain heterogeneity represented by permeability differences. The progress of the saturation front and formation and growth of fingers in time and space can be seen in more details in isosurfaces (Fig. 20).

A similar numerical simulation (*i.e.*, same geometry, initial mesh resolution, initial and boundary conditions) was also performed using dynamically adaptive mesh. During the simulation, mesh resolution ranged from 235k to 643k P<sub>1</sub>DG-P<sub>1</sub>DG element-pairs (Fig. 21a). Distinct preferable flow pathways and fingers are shown in Fig. 21b-c and 22. Saturation of the wetting fluid during the course of the simulation is shown in Fig. 23. As expected, both simulations (fixed and adaptive mesh, Figs. 18 and 23, respectively) led to similar results, *i.e.*, similar flow pathways and fingers development.

However, due to low-order accuracy of element-pairs – P<sub>1</sub>DG-P<sub>1</sub>DG instead of P<sub>1</sub>DG-P<sub>2</sub> of previous sections (for full investigation on numerical accuracy associated with these element-pairs, see Salinas et al., 2015, 2016, 2018; Adam et al., 2016; Gomes et al., 2017), and coarser mesh throughout

the computational domain, simulation performed with fixed mesh showed larger smeared fluid saturation.

## 5. Conclusions

During immiscible multi-fluid flow displacements, the expected uniform front becomes unstable due to: (a) density ratio; (b) viscosity ratio, and; (c) heterogeneity. If viscosity ratio is relatively large ( $VR \geq 3$ ), surface tension becomes weak and the interface between two fluids is unstable in the presence of tangential velocity discontinuities, leading to the formation of fingers (Saffman, 1986). Heterogeneity in the porous media domain also leads to solution instabilities in the hyperbolic Buckley-Leverett problem (Langtangen et al., 1992). This paper aims to numerically investigate the dynamics of viscous flow instabilities in porous media triggered by permeability heterogeneity.

Simulations involving formation and growth of viscous fingers were conducted with the CVFEM-based multi-fluid flow simulator Fluidity/IC-FERST model. The model is based upon a dual consistent pressure-velocity representation in CV and FEM spaces and a novel family of FE-pairs,  $P_nDG-P_m$  and  $P_nDG-P_mDG$ . Saturation and other scalar fields are discretised in CV space and may be fully discontinuous across finite element boundaries. In order to strongly enforce discretised Darcy equations at the boundaries between elements and control volumes, a directional-weighted flux-limited was introduced to take into account discontinuities risen from both, numerical formulation (based on discontinuous-Galerkin finite element method, DGFEM) and control volumes within finite elements.

The numerical formulation was initially validated against laboratory experiments (Dawe and Grattoni, 2008) to qualitatively assess model functionality to simulate crossflow (*i.e.*, preferential flow pathways) in a chequerboard permeability domain. Formation and development of viscous fingers in Hele-Shaw cells (homogeneous domain) were investigated to demonstrate that the onset of interface flow instability occur when  $VR \geq 3$ . Maximum dendritic finger widths obtained from numerical simulations performed with  $VR=10$  and  $VR=150$  largely agree with expected parametric analytic solutions (McLean and Saffman, 1981; Guan and Pitchumani, 2003). However, when perturbations are imposed into the domain's geophysical properties, *i.e.*, spatial variability of absolute permeability, numerical solutions partially agree with

analytic solutions (Table 2). This may be due to the domain homogeneity assumption in the analytic solution (Eqns. 10).

Determining the early-onset flow instability is critical to accurately simulate formation, growth and coalescence of fingers, and therefore to: (a) predict displacement (sweep) efficiency and (b) design strategies to either mitigate or avoid fingering and preferential flow pathways. Mesh resolution is thus crucial to investigate Saffmann-Taylor instabilities, and adaptive dynamic mesh technology has proved to be an efficient tool to capture initial interface perturbations. Numerical simulations were performed with VR=10 using fixed and adaptive P<sub>1</sub>DG-P<sub>2</sub> element-pairs. Results (Figs. 15 and 16) demonstrated that by dynamically adapting the mesh to follow saturation gradients (*i.e.*, fluids interfaces), early-onset flow instability and further formation of long multi-fluid fingers, which have themselves split into sub-fingers, can be readily captured (see Figs. 13i and 14i). Overall computational cost of the simulation conducted with dynamically adapting the mesh were significantly smaller than the simulation conducted with fixed mesh as indicated by the number of elements/nodes (Figs. 15).

Investigation of preferential flow pathways was the focus of Section 4.5, where 3D numerical simulations of multi-fluid flow through semi-pervious / impervious channelised domain were performed. Numerical data indicated preferential flow through regions of larger permeability leaving adjacent region (with low permeability) with nearly stagnant fluids (Figs. 18- 19). Order of accuracy of the element-pair and mesh resolution play key-roles to capture directional flow pathways and fingers in 3D simulations.

This work focuses on complexity associated with flow channelling and instability dynamics in heterogeneous porous media. Methods used to simulate such flows are based in a novel high-order CVFEM formulation that accurately preserves sharp fluid saturation gradients associated with contrasting permeability distribution. Future work will include numerical investigation of (a) crossover from capillary fingering (at low fluid velocity) to viscous fingering for immiscible unstable flows, and (b) coupled viscous and density fingering in miscible fluid flows.

## 6. Acknowledgements

Mr William Radünz would like to acknowledge the support from the Brazilian Research Council (CNPq) under the *Science without Borders scholarship programme*. Mr Konstantinos Christou would like to acknowledge the

support of the University of Aberdeen - College of Physical Science as well as the Aberdeen Formation Evaluation Society (*AFES* is an SPWLA chapter).

## References

- Adam, A., Pavlidis, D., Percival, J., Salinas, P., Xie, Z., Fang, F., Muggeridge, A., Jackson, M., 2016. Higher-order conservative interpolation between control-volume meshes: Application to advection and multiphase flow problems with dynamic mesh adaptivity. *Journal of Computational Physics* 321, 512–531.
- Alpak, F., Lake, L., Embid, S., 1999. Validation of a modified carman-kozeny equation to model two-phase relative permeabilities. In: SPE Annual Technical Conference and Exhibition. SPE, Texas, SPE56479.
- Aziz, K., Settari, A., 1986. Fundamentals of reservoir simulation. Elsevier Applied Science Publishers, New York.
- Brooks, R., Corey, A., 1964. Hydrology Papers. Vol. 3. Colorado State University Press, Ch. Hydraulic properties of porous media.
- Buckley, S., Leverett, M., 1942. Mechanism of fluid displacement in sands. *Transactions of the American Institute of Mining* 146, 107–116.
- Budek, A., Kwiatkiwski, K., Szymczak, P., 2017. Effect of mobility ratio on interaction between teh fingers in unstable growth processes. *Physical Review E* 96, 042218.
- Carvalho, G. D., Miranda, J. A., Gadêlha, H., Nov 2013. Interfacial elastic fingering in Hele-Shaw cells: A weakly nonlinear study. *Phys. Rev. E* 88, 053006.
- Chang, Y., Pope, G., K.Seperhnoori, 1990. A higher-order finite difference compositional simulator. *Journal of Petroleum Science and Engineering* 5, 35–50.
- Chavent, G., Jaffré, J., 1986. Mathematical Models and Finite Elements for Reservoir Simulation. Vol. 17 of Studies in Mathematics and Its Applications. North Holland.
- Chen, Z., Huan, G., Ma, Y., 2006. Computational Methods for Multiphase Flows in Porous Media. SIAM.

- Chen, Z., Huan, G., Wang, H., 2005. Simulation of a compositional model for multiphase flow in porous media. *Numerical Methods for Partial Differential Equations* 21 (4), 726–741.
- Cotter, C., Ham, D., C.C, P., Reich, S., 2009. LBB stability of a mixed discontinuous/continuous galerkin finite element pair. *Journal of Computational Physics* 228, 336–348.
- Courant, R., Friedrichs, K., Lewy, H., 1941. On difference equations of mathematical physics. *Uspekhi Mat. Nauk* 8, 125–160.
- Cumming, B., 2012. Modelling sea water intrusion in coastal aquifers using heterogeneous computing. Ph.D. thesis, Queensland University of Technology, Australia.
- Cumming, B., Moroney, T., Turner, I., 2011. A mass-conservative control volume-finite element method for solving Richards' equation in heterogeneous porous media. *BIT Numerical Mathematics* 51 (4), 845–864.
- Dawe, R., Grattoni, C., 2008. Experimental displacement patterns in a  $2 \times 3$  quadrant block with permeability and wettability heterogeneities problems for numerical modelling. *Transport in Porous Media* 71, 5–22.
- Evans, R., Dawe, R., 1994. The danger of neglecting nodal crossflow in heterogeneous near-wellbore conditions. *Journal of Petroleum Science and Engineering* 11 (2), 113–121.
- Frey, P., George, P.-L., 2008. Mesh Generation, 2nd Edition. Wiley.
- Fung, L., Hiebert, A., Nghiem, L., 1992. Reservoir simulation with control-volume finite element method. *SPE Reservoir Engineering* 7 (3), 349–357.
- Gomes, J., Pavlidis, D., Salinas, P., Percival, J., Xie, Z., Melnikova, Y., Pain, C., Jackson, M., 2017. A force balanced control volume finite element method for multi-phase porous media flow modelling. *Int. J. Numer. Methods in Fluids* 83, 431–455.
- Gomes, J., Tollit, B., Milles, B., Pain, C., 2012. Fluidization Engineering – Principles and Practice. National University of Singapore, Singapore, Ch. Multi-Physics Flow Modelling for Nuclear Applications.

- Guan, X., Pitchumani, R., 2003. Viscous fingering in a Hele-Shaw cell with finite viscosity ratio and interfacial tension. *Transactions of the ASME* 125, 354–364.
- Habermann, B., 1960. The efficiency of miscible displacements as a function of mobility ratio. *Petroleum Transactions, AIME* 219, 264–272.
- Hiester, H., Piggott, M., Farrell, P., Allison, P., 2014. Assessment of spurious mixing in adaptive mesh simulations of the two-dimensional lock exchange. *Ocean Modelling* 73, 30–44.
- Homsy, G., 1987. Viscous fingering in porous media. *Ann. Rev. Fluid Mechanics* 19, 271–311.
- Howison, S. D., 2000. A note on the two-phase Hele-Shaw problem. *Journal of Fluid Mechanics* 409, 243–249.
- Jackson, M., Gomes, J., Mostaghimi, P., Percival, J., Tollit, B., Pavlidis, D., Pain, C., El-Sheikh, A., Muggeridge, A., Blunt, M., 2013. Reservoir modeling for flow simulation using surfaces, adaptive unstructured meshes, and control-volume-finite-element methods. In: *SPE Reservoir Simulation Symposium*.
- Jackson, M., Percival, J., Mostaghimi, P., Tollit, B., Pavlidis, D., Pain, C., Gomes, J., ElSheikh, A., Salinas, P., Muggeridge, A., Blunt, M., 2015. Reservoir modeling for flow simulation by use of surfaces, adaptive unstructured meshes, and an overlapping-control-volume finite-element method. *SPE Reservoir Evaluation & Engineering* 18 (2), SPE-163633-PA.
- Jackson, S., Power, H., Giddings, D., Stevens, D., 2017. The stability of immiscible viscous fingering in Hele-Shaw cells with spatially varying permeability. *Computer Methods in Applied Mechanics and Engineering* 320, 606 – 632.
- Jiang, X., 2011. A review of physical modelling and numerical simulation of long-term geological storage of carbon dioxide. *Applied Energy* 88, 3557–3566.
- King, M., Mansfield, M., 1999. Flow simulation of geologic models. *SPE Reservoir Evaluation & Engineering* SPE-57469-PA.

- Kirkland, M., Hills, R., Wierenga, P., 1992. Algorithms for solving Richards' equation for variably-saturated soils. *Water Resources Research* 28, 2049–2058.
- Langtangen, H., Tveito, A., Winther, R., 1992. Instability of Buckley-Leverett flow in a heterogeneous medium. *Transport in Porous Media* 9, 165–185.
- Lo, S., 2015. Finite Element Mesh Generation. CRC Press.
- Lux, J., Anguy, Y., 2012. A study of the behavior of implicit pressure explicit saturation (IMPES) schedules for two-phase flow in dynamic pore network models. *Transp. Porous Med.* 93, 203–221.
- McLean, J., Saffman, P., 1981. The effect of surface tension on the shape of fingers in a Hele-Shaw cell. *J. Fluid Mechanics* 102, 455–469.
- Melnikova, Y., Jacquemyn, C., Osman, H., Salinas, P., Gorman, G., Hampson, G., Jackson, M., 2016. Reservoir modelling using parametric surfaces and dynamically adaptive fully unstructured grids. In: Proceedings of the XV European Conference on the Mathematics of Oil Recovery (ECMOR XV). EAGE.
- Mlacnik, M., Durlofsky, L., Heinemann, Z., 2004. Dynamic flow-based PEBI grids for reservoir simulation. SPE 90009.
- Mostaghimi, P., Kamall, F., Jackson, M., Muggeridge, A., Pain, C., 2016. Adaptive mesh optimisation for simulation of immiscible viscous fingering. *SPE Journal* 21, 250–259.
- Muskat, M., 1934. Two fluid systems in porous media. the encroachment of water into an oil sand. *Journal of Applied Physics* 5, 250–264.
- Nick, H., Matthai, S., 2011a. Comparison of three FE-FV numerical schemes for single- and tw-phase flow simulation of fractured porous media. *Transp. Porous Med* 90, 421–444.
- Nick, H., Matthai, S., 2011b. A hybrid finite-element finite-volume method with embedded discontinuities for solute transport in heterogeneous media. *Vadose Zone Journal* 10, 299–312.

- Nicolaides, C., Jha, B., Cueto-Felgueroso, L., Juanes, R., 2015. Impact of viscous fingering and permeability heterogeneity on fluid mixing porous media. *Water Resources Research* 51, WR015811.
- Pain, C., Umpleby, A., de Oliveira, C., Goddard, A., 2001. Tetrahedral mesh optimisation and adaptivity for steady-state and transient finite element calculations. *Computer Methods in Applied Mechanics and Engineering* 190, 3771–3796.
- Paluszny, A., Matthai, S., Hohmeyer, M., 2007. Hybrid finite element finite volume discretization of complex geologic structures and a new simulation workflow demonstrated on fractured rocks. *Geofluids* 7, 186–208.
- Pavlidis, D., Gomes, J., Xie, Z., Percival, J., Pain, C., Matar, O., 2016. Compressive advection and multi-component methods for interface-capturing. *International Journal for Numerical Methods in Fluids* 80 (4), 256–282.
- Pietro, D. D., Vohralík, M., Yousef, S., 2014. An a posteriori-based, fully adaptive algorithm with adaptive stopping criteria and mesh refinement for thermal multiphase compositional flows in porous media. *Computers and Mathematics with Applications* 68 (12B), 2331–2347.
- Piggott, M., Pain, C., Gorman, G., Power, P., Goddard, A., 2006. h,r and hr adaptivity with application in numerical ocean modelling. *Ocean Modelling* 10, 95–113.
- Plewa, T., Linde, T., Weirs, V. (Eds.), 2004. Adaptive Mesh Refinement – Theory and Applications. Vol. 41 of Lecture Notes in Computational Science and Engineering. Springer.
- Power, P., Piggott, M., Fang, F., Gorman, G., Pain, C., Marshall, D., Goddard, A., 2006. Adjoint goal-based error norms for adaptive mesh ocean modelling. *Ocean Modelling* 15, 3–38.
- Praud, O., Swinney, H. L., Jul 2005. Fractal dimension and unscreened angles measured for radial viscous fingering. *Phys. Rev. E* 72, 011406.
- Radünz, W., Oliveira, F., Gomes, J., July 2014. A multi-scale model of multi-fluid flows transport in dual saturated-unsaturated heterogeneous

- porous media. In: Onate, E., Oliver, J., Huerta, A. (Eds.), Proceedings of the XI World Congress on Computational Mechanics (WCCM XI). IACM/ECCOMAS, Barcelona, Spain.
- Riaz, A., Tchelepi, H. A., 2004. Linear stability analysis of immiscible two-phase flow in porous media with capillary dispersion and density variation. *Physics of Fluids* 16 (12), 4727–4737.
- Saffman, P., 1959. Theory of dispersion in porous medium. *J. Fluid Mechanics* 6, 321–349.
- Saffman, P., 1986. Viscous fingering in Hele-Shaw cells. *J. Fluid Mechanics* 173, 73–94.
- Saffman, P., Taylor, G. I., 1958. The penetration of a fluid into a porous medium or Hele-Shaw cell containing a more viscous liquid. *Proc. R. Soc. London A* 245, 321–329.
- Salinas, P., Pavlidis, D., Xie, Z., Adam, A., Pain, C., Jackson, M., 2016. Improving the convergence behaviour of a fixed-point-iteration solver for multiphase flow in porous media. *International Journal for Numerical Methods in Fluids* 84, 466–476.
- Salinas, P., Pavlidis, D., Xie, Z., Osman, H., Pain, C., Jackson, M., 2018. A discontinuous control volume finite element method for multiphase flow in heterogeneous porous media. *Journal of Computational Physics* 352, 602–614.
- Salinas, P., Percival, J., Pavlidis, D., Xie, Z., Gomes, J., Pain, C., Jackson, M., et al., 2015. A discontinuous overlapping control volume finite element method for multi-phase porous media flow using dynamic unstructured mesh optimization. In: SPE-173279-MS, Reservoir Simulation Symposium. Society of Petroleum Engineers.
- Self, S., Reddy, B., Rosen, M., 2012. Review of underground coal gasification technologies and carbon capture. *International Journal of Energy and Environmental Engineering* 3, 16–24.
- Sheldon, J., Cardwell, W., 1959. One-dimensional, incompressible, noncapillary two-phase fluid flow in a porous media. *Petroleum Transactions, AIME* 216.

- Spycher, N., Pruess, K., Ennis-King, J., 2003. CO<sub>2</sub>-H<sub>2</sub>O mixtures in the geological sequestration of CO<sub>2</sub>. II. Assessment and calculation of mutual solubilities from 12 to 100°C and up to 600 bar. *Geochim. Cosmochim. Acta* 67 (16), 2015–3031.
- Su, K., Latham, J., Pavlidis, D., Xiang, J., Fang, F., Mostaghimi, P., Percival, J., Pain, C., Jackson, M., 2016. Multiphase flow simulation through porous media with explicitly resolved fractures. *Geofluids* 15, 592–607.
- Tabeling, P., Zocchi, G., Libchaber, A., 1987. An experimental study of the Saffman-Taylor instability. *Journal of Fluid Mechanics* 177, 67–82.
- Tan, C., Homsy, G., 1988. Simulation of nonlinear viscous fingering in miscible displacement. *Physics of Fluids* 31, 1330–1338.
- Tavassoli, S., Pope, G. A., Sepehrnoori, K., et al., 2015. Frontal-stability analysis of surfactant floods. *SPE Journal* 20 (03), 471–482.
- Tchelepi, H., Jr, F. O., 1994. Interaction of viscous fingering, permeability heterogeneity and gravity segregation in three dimensions. *SPE* 25235, 266–271.
- Voller, V., 2009. Basic Control Volume Finite Element Methods for Fluids and Solids. Vol. 1 of IISc Research Monographs Series. World Scientific Publishing Co, Singapore.
- White, I., Lewis, R., W, L, W., 1981. The numerical simulation of multiphase flow through a porous medium and its application to reservoir engineering. *Applied Mathematical Modelling* 5, 165–172.
- Wing, R., Russel, T., Young, L., 1989. An anisotropic coarse-grid dispersion model of heterogeneity and viscous fingering in five-spot miscible displacement that matches experiments and fine-grid simulations. *SPE* 18441, 447–465.
- Wooding, R. A., Morel-Seytoux, 1976. Multiphase fluid flow through porous media. *Ann. Rev. Fluid Mechanics* 8, 233–274.

## List of Tables

1	Sumary of model set-up used in the numerical simulations. Superscript $\circ$ denotes initial condition. $\mathbf{K}_i$ is in $cm^2$ and $u_w^\circ$ is in $cm.s^{-1}$ . $S_{w,irr}$ and $S_{nw,r}$ are the same for all simulations. <b>KOSTAS: PLEASE MAKE SURE THAT ALL DATA IS UPDATED...</b>	28
2	Flow simulations in Heleshaw cells (Section 4.3): summary of finger width calculations using Eqn. 10 and obtained through numerical simulations. $\lambda_f^{calc}$ was calculated based on fingers' tip velocities and outflow rate. Calculations were based on simulation data obtained from snapshots shown in Fig. 8.	29

Section	$\phi$	VR	$S_w^\circ$	$S_{nw}^\circ$	$\mathbf{K}_1$	$\mathbf{K}_2$	$\mathbf{K}_3$	$\mathbf{K}_4$	$S_{w,irr}$	$S_{nw,r}$	$u_w^\circ$
4.2	0.2	1.0	0.0	1.0	2.5	1.0	N/A	N/A	0.2	0.3	1.0
4.3(homogenous)	0.2	10.0	0.0	1.0	1.e-10	N/A	N/A	N/A	0.2	0.3	0.5
4.3(heterogenous)	0.2	1.0	0.0	1.0	1.0e-11 – 5.0e-10	1.0e-12 – 5.0e-10	1.0e-12 – 1.0e-10	1.0e-10	0.2	0.3	1.0
4.4	0.2	1.0	0.0	1.0	3.0	2.0	5.0	1.0	0.2	0.3	0.5
4.5	0.2	1.0	0.0	1.0	3.0	2.0	5.0	1.0	0.2	0.3	0.5

Table 1: Sumary of model set-up used in the numerical simulations. Superscript  $\circ$  denotes initial condition.  $\mathbf{K}_i$  is in  $cm^2$  and  $u_w^\circ$  is in  $cm.s^{-1}$ .  $S_{w,irr}$  and  $S_{nw,r}$  are the same for all simulations. **KOSTAS: PLEASE MAKE SURE THAT ALL DATA IS UPDATED...**

	<b>K</b> (cm <sup>2</sup> )	<i>VR</i>	$\lambda_f^{(\text{calc,max})}$ (cm) (Eqn. 10)	$\lambda_f^{(\text{simul,max})}$ (cm)
<b>Case 1</b> (homogeneous)	$1 \times 10^{-10}$	10	0.13-0.75	0.45-0.70
<b>Case 2</b> (homogeneous)	$1 \times 10^{-10}$	150	0.30-0.75	0.50-0.90
<b>Case 3</b> (heterogeneous)	$1 \times 10^{-12}$ - $5 \times 10^{-10}$	10	0.25-4.50	0.44-0.56
<b>Case 4</b> (heterogeneous)	$1 \times 10^{-12}$ - $5 \times 10^{-10}$	150	0.88-3.00	0.24-0.40

Table 2: Flow simulations in Heleshaw cells (Section 4.3): summary of finger width calculations using Eqn. 10 and obtained through numerical simulations.  $\lambda_f^{\text{calc}}$  was calculated based on fingers' tip velocities and outflow rate. Calculations were based on simulation data obtained from snapshots shown in Fig. 8.

## List of Figures

1	2D representation of $P_1$ DG- $P_2$ element pairs used in this work. Shaded areas denote control volumes across two contiguous elements. Blue and white circles represent pressure and velocity nodes, respectively. . . . .	33
2	Graphical representation of two different element-types: triangles $A$ and $B$ represent $P_1$ DG- $P_2$ and $P_1$ DG- $P_1$ element-pairs, respectively. Porosity $\phi_i$ , permeability $\mathbf{K}_i$ , velocity and pressure are represented in FE space whereas scalar fields (such as saturation, density, viscosity etc) are represented in CV space. . . . .	34
3	Schematics of formation of flow instabilities during injection of a pure low viscosity fluid (red) into a domain saturated with a second fluid (dark blue). The viscosity ratio of the two fluids is $VR=5$ . In this case, the initially piston shape front collapses leading to the formation of several fingers. . . . .	35
4	Model validation of fluid displacement in heterogeneous porous media ( $VR=1$ ): (a) the domain is divided into four subdomains with prescribed synthetic permeability, $\mathbf{K}_1 = 1$ and $\mathbf{K}_2 = 2.5$ ; (b-c) snapshots of saturation (displacing fluid) field at $t=25$ and $t=300$ . The domain is discretised with 5960 $P_1$ DG- $P_2$ elements. . . . .	36
5	Simulated flow in a Hele-Shaw cell ( $VR=3$ , $\mathbf{K}=10^{-10}\text{cm}^2$ ): (a) initial pressure profile (in $\text{g.cm}^{-1}.\text{s}^{-2}$ ) with source and sink regions explicitly shown along with dimensions (in cm); (b-f) snapshots of wetting phase saturation showing flow profile as the simulation evolves. The domain contains 26313 $P_1$ DG- $P_2$ triangular elements. . . . .	37
6	Simulated flow in a Hele-Shaw cell ( $VR=10$ , $\mathbf{K}=10^{-10}\text{cm}^2$ ): snapshots of overlapped wetting phase saturation and velocity vectors (in $\text{cm.s}^{-1}$ ) showing flow profile as the simulation evolves. The domain contains 26313 $P_1$ DG- $P_2$ triangular elements. . . . .	38
7	Simulated flow in a Hele-Shaw cell ( $VR=150$ , $\mathbf{K}=10^{-10}\text{cm}^2$ ): snapshots of wetting phase saturation showing flow profile as the simulation evolves. The domain contains 26313 $P_1$ DG- $P_2$ triangular elements. . . . .	39

8	Isosurfaces of simulated flows in Hele-Shaw cells with viscosity ratios of 10 (a and c) and 150 (b and d). Top and bottom rows describe simulations performed with constant <i>i.e.</i> <i>homogeneous</i> with $K = 10^{-10} \text{ cm}^2$ and randomly distributed ( <i>i.e.</i> heterogeneous, Fig. 9a) permeabilities. Width of largest fingers for homogeneous cases are approximately 0.70 and 0.90cm ( $VR=10$ and $VR=150$ , respectively), whereas for heterogeneous cases are 0.56 and 0.40cm. Results for homogeneous cases are in good agreement with values obtained from Guan and Pitchumani (2003)'s analytic solution. . . . .	40
9	Simulated flow in a modified Hele-Shaw cell with $VR=10$ : (a) permeability distribution ( $10^{-10} \leq K_1 \leq 5 \times 10^{-10}$ , $K_2=10^{-10}$ , $10^{-11} \leq K_3 \leq 5 \times 10^{-10}$ and $10^{-12} \leq K_4 \leq 5 \times 10^{-10} \text{ cm}^2$ ); (b-f) snapshots of saturation profile during 9.77 seconds of simulation. The domain contains 26313 P <sub>1</sub> DG-P <sub>2</sub> element-pairs. . . . .	41
10	Simulated flow in a modified Hele-Shaw cell with $VR=150$ : snapshots of saturation profile during 2.50 seconds of simulation. Permeability distribution used in this simulation was the same as shown in Fig. 9a. The domain contains 26313 P <sub>1</sub> DG-P <sub>2</sub> element-pairs. . . . .	42
11	Simulated flow in a modified Hele-Shaw cell with $VR=150$ : snapshots of saturation profile. Permeability distribution used in this simulation was the same as shown in Fig. 9a. The domain contains 3734 P <sub>1</sub> DG-P <sub>2</sub> element-pairs. . . . .	43
12	Impact of mesh resolution on capturing flow instabilities: (a) permeability and (b) initial saturation and mesh resolution used in the simulations performed in Section 4.4. There are 13068 P <sub>1</sub> DG-P <sub>2</sub> element-pairs in the domain. . . . .	44
13	Impact of mesh resolution on capturing flow instabilities: snapshots of saturation field through 1.50 seconds of numerical simulation performed with fixed mesh (of 13068 elements) and $VR=10$ . . . . .	45
14	Impact of mesh resolution on capturing flow instabilities: snapshots of saturation field through 1.50 seconds of numerical simulation performed with adaptive mesh and $VR=10$ . . . . .	46

15	Impact of mesh resolution on capturing flow instabilities: total number of elements (red) and nodes (blue) for simulations performed with fixed (dotted line) and adaptive (full line) mesh.	47
16	Impact of mesh resolution on flow instabilities: capturing formation and growth of flow instabilities at fluid interfaces ( $t = 0.20$ s) in two regions of the computational domain, <i>A</i> and <i>B</i> . Simulations were conducted with fixed (left-hand side) and adaptive meshes.	48
17	3D channel flow: Permeability distribution within the computational domain, containing 235242 P <sub>1</sub> DG-P <sub>1</sub> DG element-pairs.	49
18	3D channel flow (fixed mesh): saturation front evolving in time and space with preferential flow pathways through 3.50 seconds of numerical simulations. Preferential flow pathway can be readily noticed in these frames, mirroring permeability distribution. The domain contains 235242 P <sub>1</sub> DG-P <sub>1</sub> DG elements.	50
19	3D channel flow (fixed mesh): XY and YZ planes showing wetting phase saturation overlapped with Darcy velocity vectors (in cm.s <sup>-1</sup> ) at (a) $t=0.29$ s and (b) $t=4.3$ s.	51
20	3D channel flow (fixed mesh): Isosurfaces for wetted phase saturation ranging from 0.45 and 0.60 at the same instants of time of Fig. 18. Preferential flow pathway can be readily noticed in (b) and (f). Fingers' formation and growth can be clearly noticed in (b)-(e). The domain contains 235242 P <sub>1</sub> DG-P <sub>1</sub> DG elements.	52
21	3D Channel (adaptive mesh): (a) Wetting fluid saturation overlapped with mesh; (b) streamlines and; (c) isosurfaces. All plots are shown at 3.78s (Fig. 22f).	53
22	3D Channel (adaptive mesh): XY and YZ planes showing wetting fluid saturation overlapped with Darcy velocity vectors at (a) 0.00, (b) 0.09, (c) 0.71, (d) 1.75, (e) 2.47 and (f) 3.78s. Colour scheme for saturation profile is the same as used in Fig. 23.	54
23	3D channel flow (adaptive mesh): numerical simulation was performed with the smae boundary and initial conditions as in Figs. 17-20 with an adaptive mesh. Flow pathway is very similar to the one shown in Fig. 18.	55

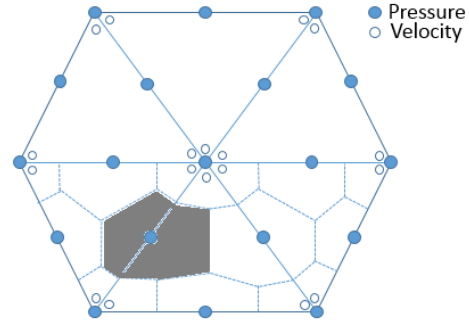


Figure 1: 2D representation of  $P_1$ DG- $P_2$  element pairs used in this work. Shaded areas denote control volumes across two contiguous elements. Blue and white circles represent pressure and velocity nodes, respectively.

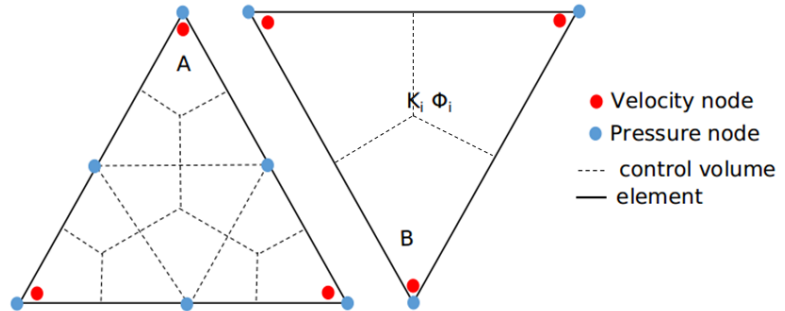


Figure 2: Graphical representation of two different element-types: triangles  $A$  and  $B$  represent  $P_1$ DG- $P_2$  and  $P_1$ DG- $P_1$  element-pairs, respectively. Porosity  $\phi_i$ , permeability  $\mathbf{K}_i$ , velocity and pressure are represented in FE space whereas scalar fields (such as saturation, density, viscosity etc) are represented in CV space.

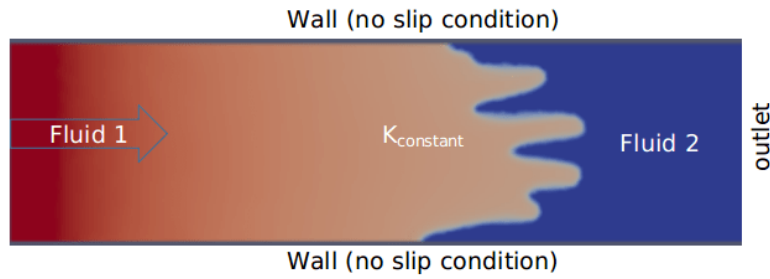
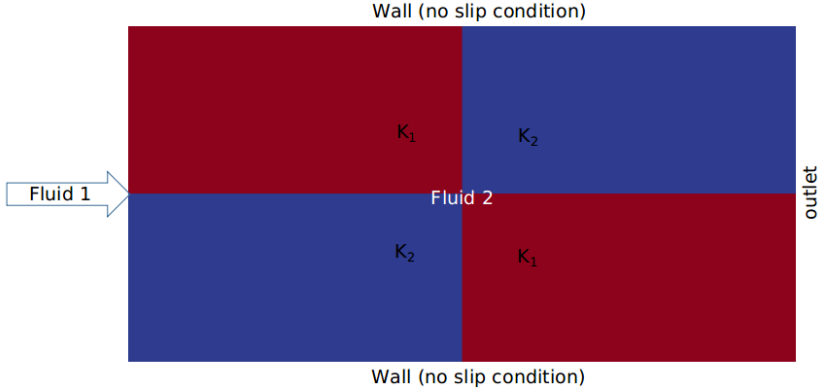
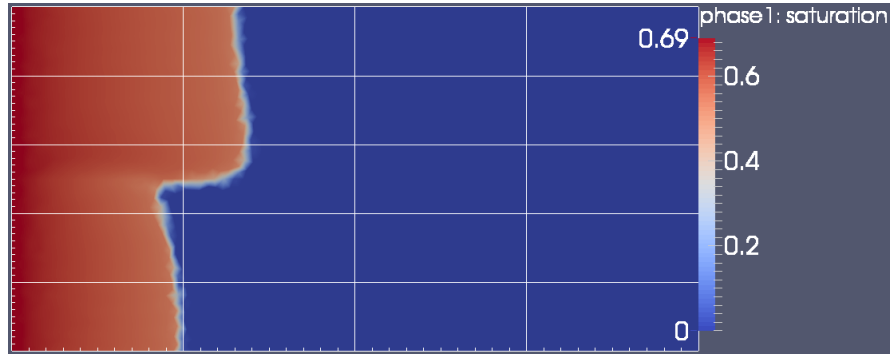


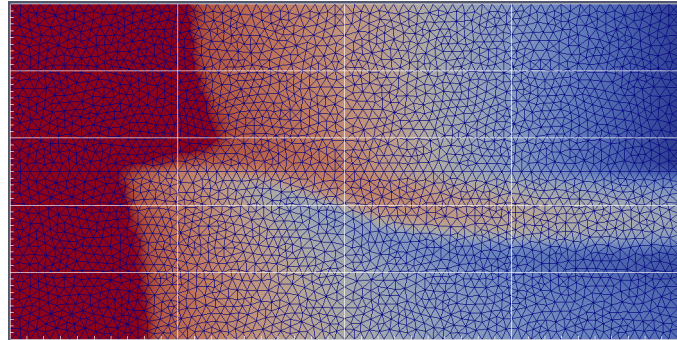
Figure 3: Schematics of formation of flow instabilities during injection of a pure low viscosity fluid (red) into a domain saturated with a second fluid (dark blue). The viscosity ratio of the two fluids is  $\text{VR}=5$ . In this case, the initially piston shape front collapses leading to the formation of several fingers.



(a) Schematics of the domain with permeability ( $\mathbf{K}$ ) distribution



(b) flow at  $t=25$



(c) flow at  $t=3000$

Figure 4: Model validation of fluid displacement in heterogeneous porous media ( $VR=1$ ): (a) the domain is divided into four subdomains with prescribed synthetic permeability,  $\mathbf{K}_1 = 1$  and  $\mathbf{K}_2 = 2.5$ ; (b-c) snapshots of saturation (displacing fluid) field at  $t=25$  and  $t=300$ . The domain is discretised with 5960  $P_1$ DG- $P_2$  elements.

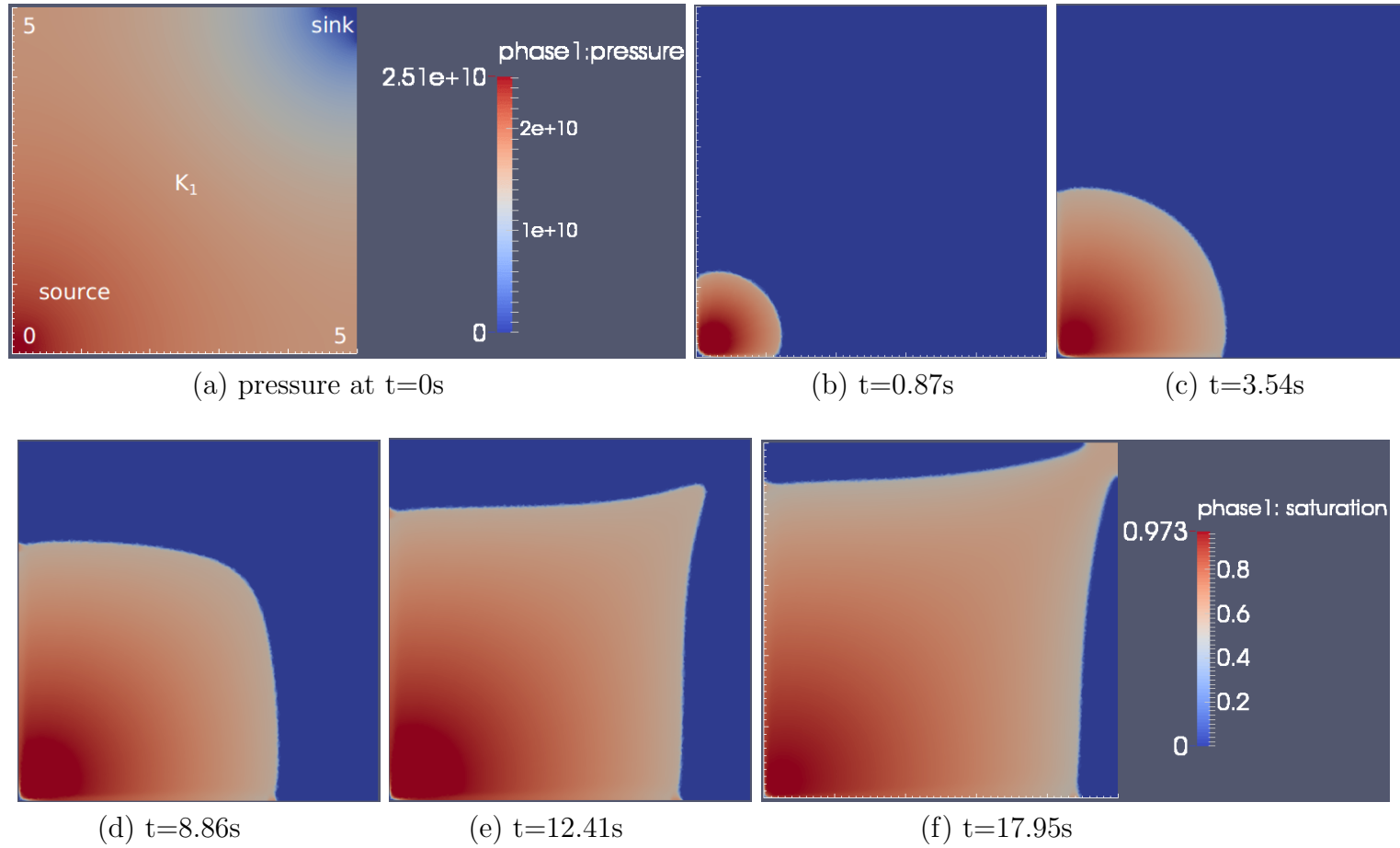


Figure 5: Simulated flow in a Hele-Shaw cell ( $VR=3$ ,  $K=10^{-10} \text{cm}^2$ ): (a) initial pressure profile (in  $\text{g.cm}^{-1}.\text{s}^{-2}$ ) with source and sink regions explicitly shown along with dimensions (in cm); (b-f) snapshots of wetting phase saturation showing flow profile as the simulation evolves. The domain contains 26313  $P_1$ DG- $P_2$  triangular elements.

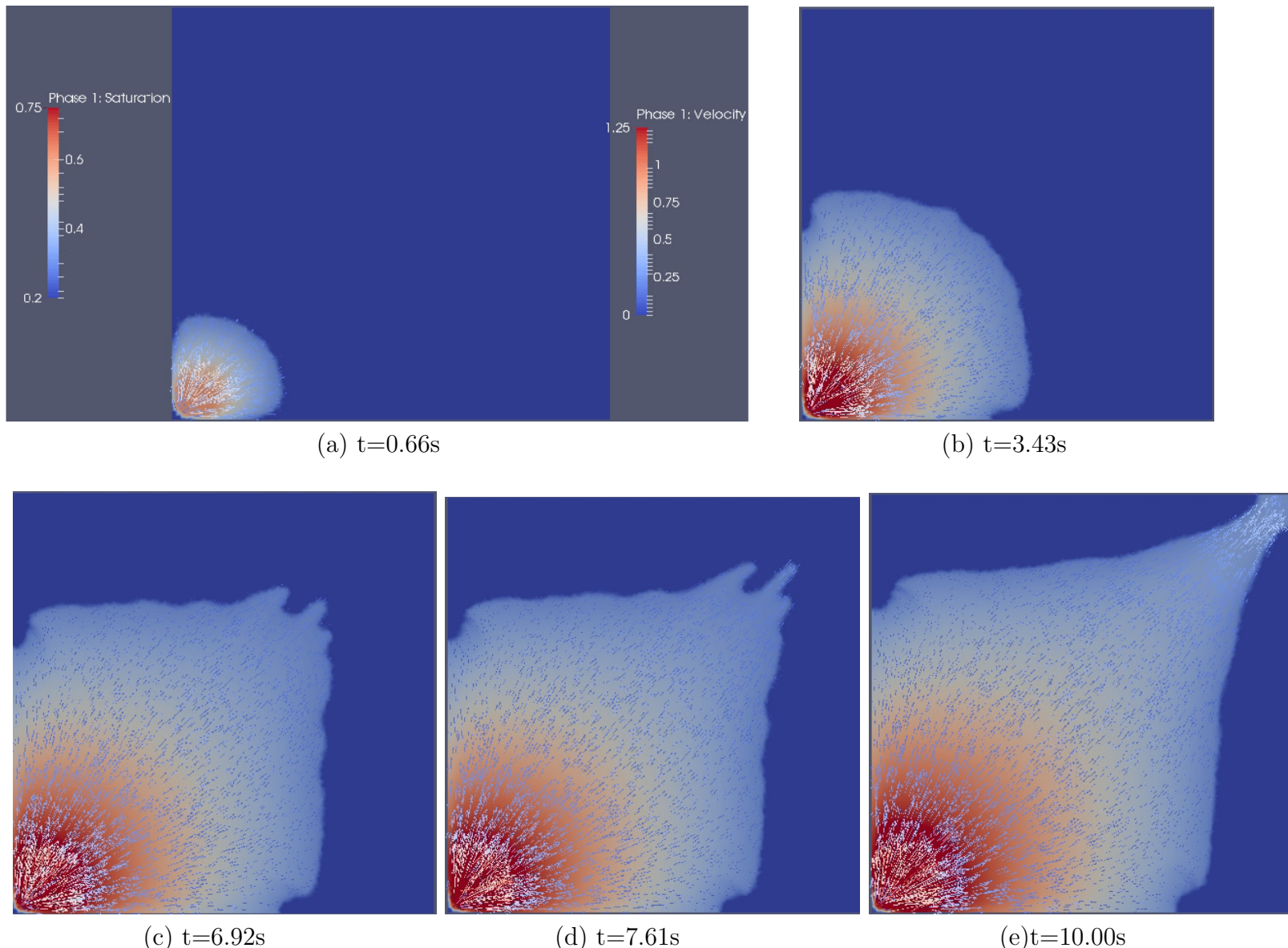


Figure 6: Simulated flow in a Hele-Shaw cell ( $VR=10$ ,  $\mathbf{K}=10^{-10}\text{cm}^2$ ): snapshots of overlapped wetting phase saturation and velocity vectors ( $\text{in cm.s}^{-1}$ ) showing flow profile as the simulation evolves. The domain contains 26313  $P_1\text{DG}-P_2$  triangular elements.

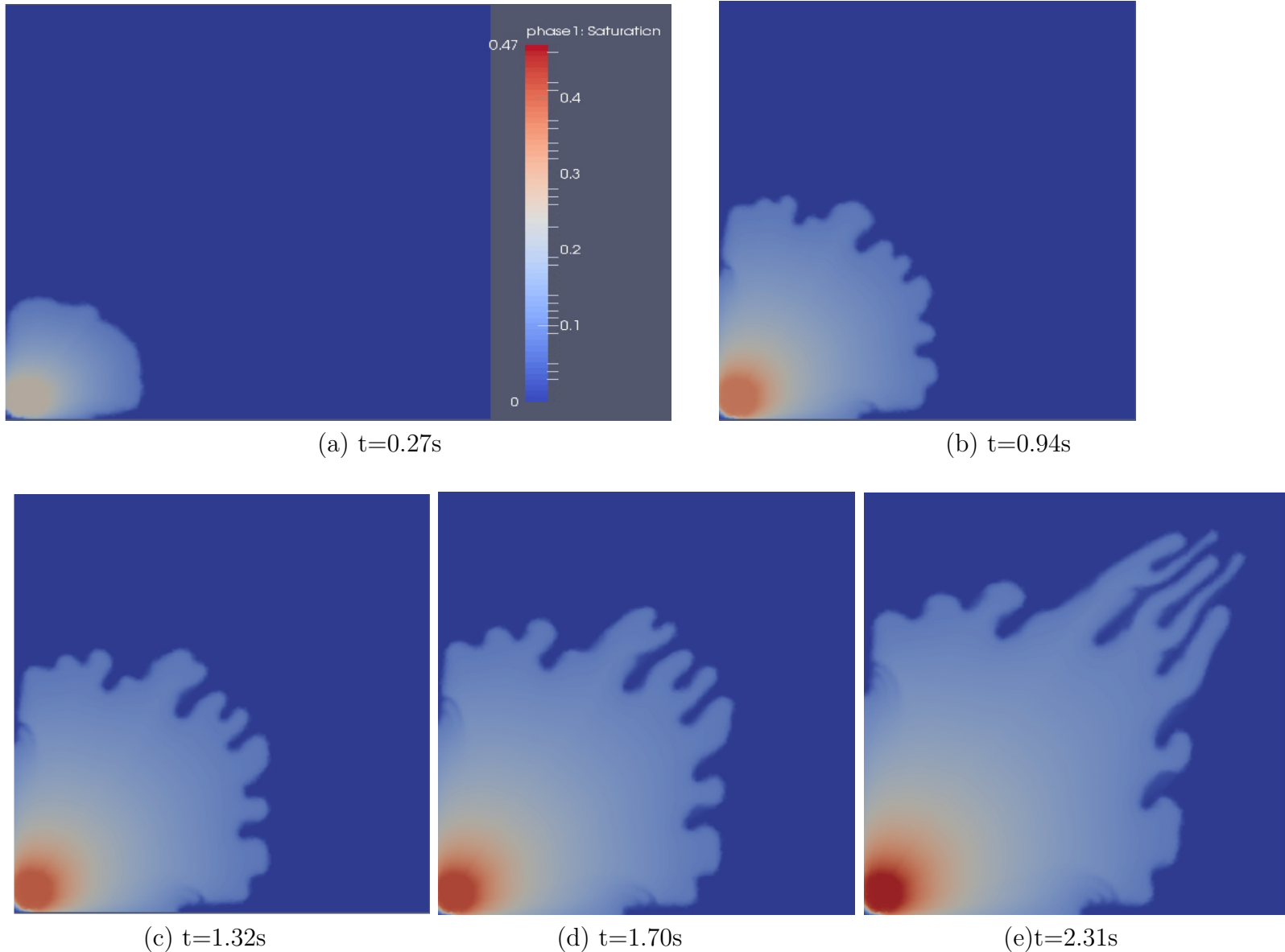


Figure 7: Simulated flow in a Hele-Shaw cell ( $VR=150$ ,  $\mathbf{K}=10^{-10}\text{cm}^2$ ): snapshots of wetting phase saturation showing flow profile as the simulation evolves. The domain contains 26313  $P_1\text{DG}-P_2$  triangular elements.

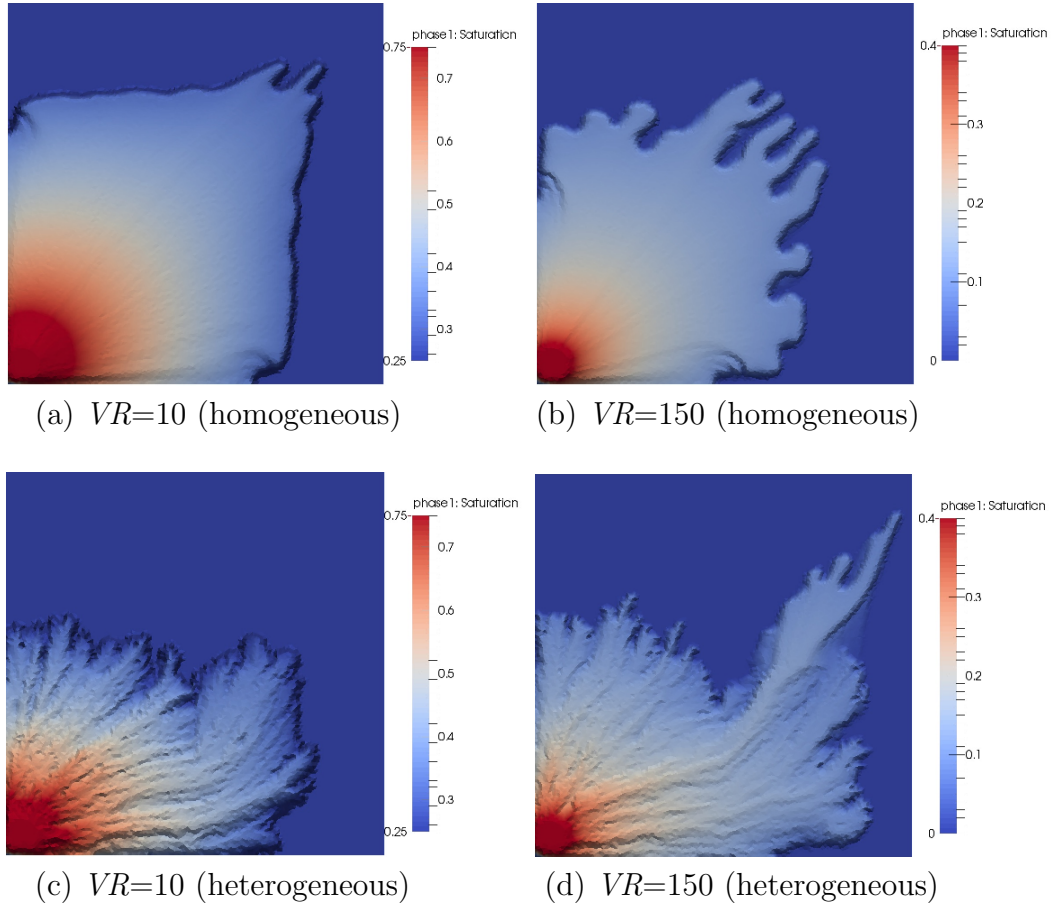


Figure 8: Isosurfaces of simulated flows in Hele-Shaw cells with viscosity ratios of 10 (a and c) and 150 (b and d). Top and bottom rows describe simulations performed with constant *i.e.* *homogeneous with*  $\mathbf{K} = 10^{-10} \text{ cm}^2$  and randomly distributed (*i.e.* heterogeneous, Fig. 9a) permeabilities. Width of largest fingers for homogeneous cases are approximately 0.70 and 0.90cm ( $VR=10$  and  $VR=150$ , respectively), whereas for heterogeneous cases are 0.56 and 0.40cm. Results for homogeneous cases are in good agreement with values obtained from [Guan and Pitchumani \(2003\)](#)'s analytic solution.

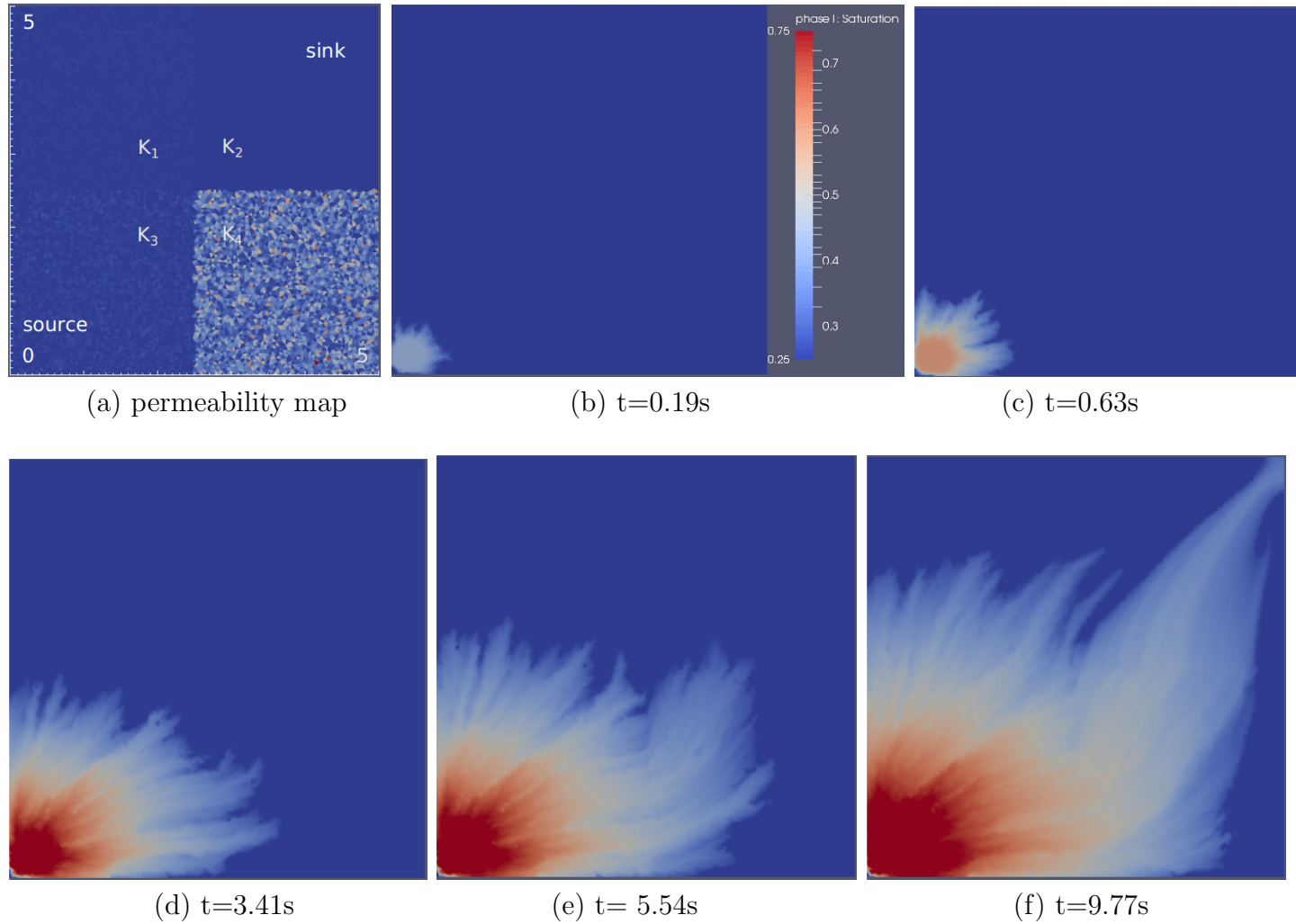


Figure 9: Simulated flow in a modified Hele-Shaw cell with  $VR=10$ : (a) permeability distribution ( $10^{-10} \leq \mathbf{K}_1 \leq 5 \times 10^{-10}$ ,  $\mathbf{K}_2=10^{-10}$ ,  $10^{-11} \leq \mathbf{K}_3 \leq 5 \times 10^{-10}$  and  $10^{-12} \leq \mathbf{K}_4 \leq 5 \times 10^{-10} \text{ cm}^2$ ); (b-f) snapshots of saturation profile during 9.77 seconds of simulation. The domain contains 26313 P<sub>1</sub>DG-P<sub>2</sub> element-pairs.

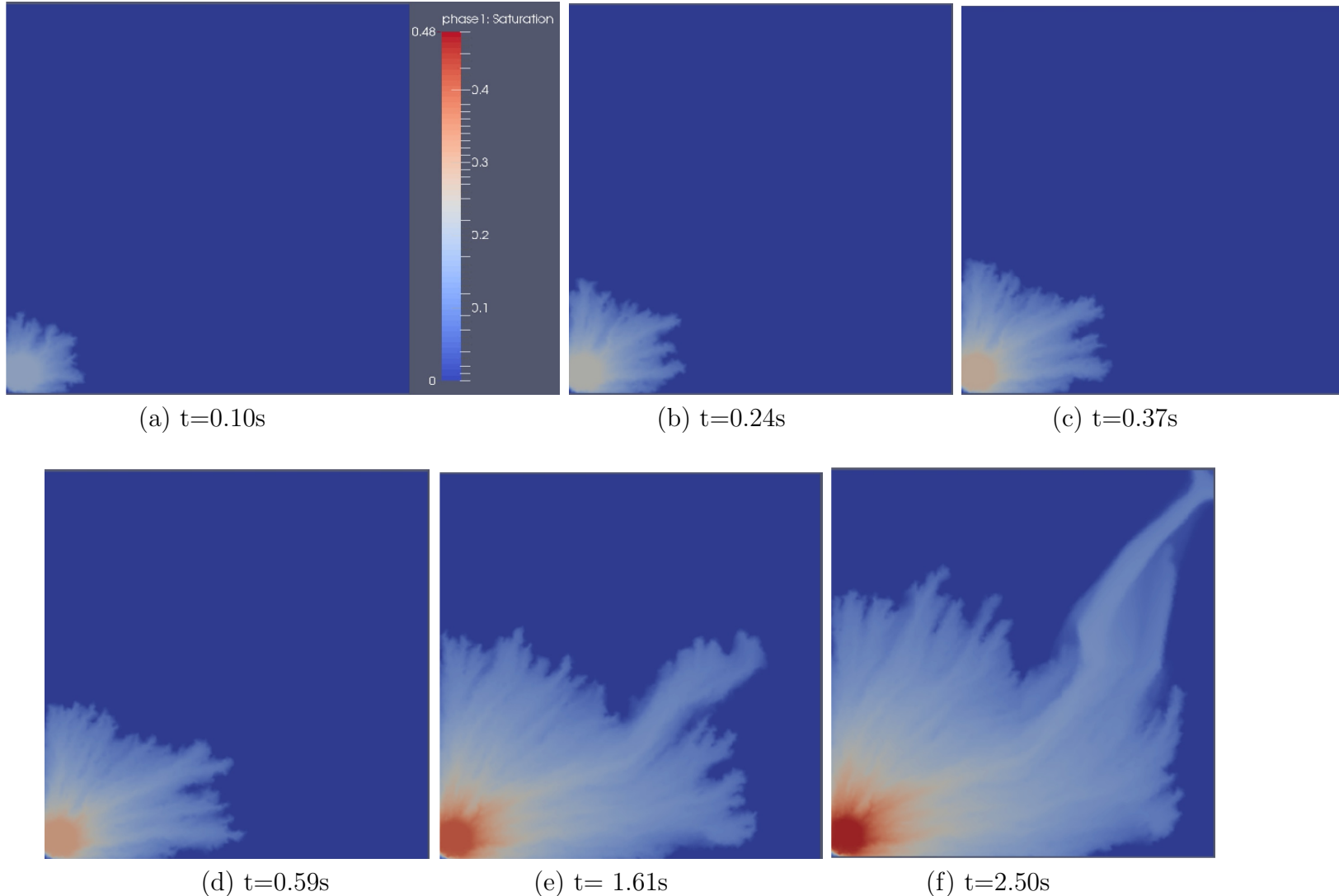


Figure 10: Simulated flow in a modified Hele-Shaw cell with  $VR=150$ : snapshots of saturation profile during 2.50 seconds of simulation. Permeability distribution used in this simulation was the same as shown in Fig. 9a. The domain contains 26313  $P_1$ DG- $P_2$  element-pairs.

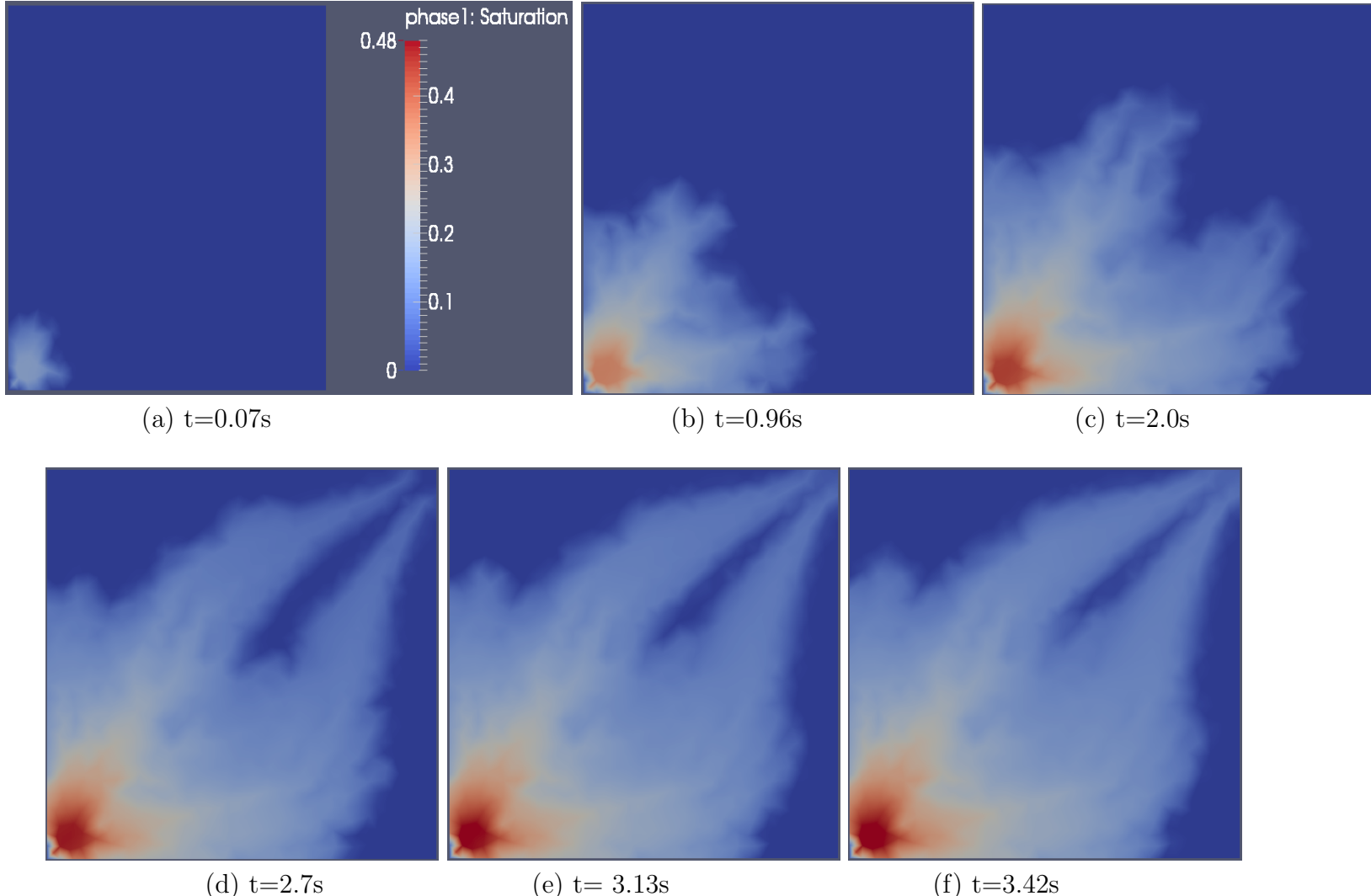
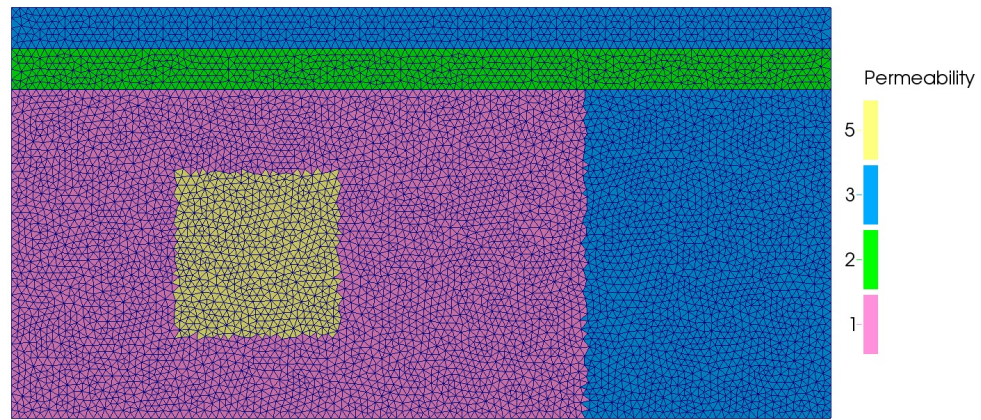


Figure 11: Simulated flow in a modified Hele-Shaw cell with  $VR=150$ : snapshots of saturation profile. Permeability distribution used in this simulation was the same as shown in Fig. 9a. The domain contains 3734 P<sub>1</sub>DG-P<sub>2</sub> element-pairs.



(a) Permeability mapping ( $\mathbf{K}$ )



(b) Initial saturation distribution

Figure 12: Impact of mesh resolution on capturing flow instabilities: (a) permeability and (b) initial saturation and mesh resolution used in the simulations performed in Section 4.4. There are 13068  $P_1$ DG- $P_2$  element-pairs in the domain.

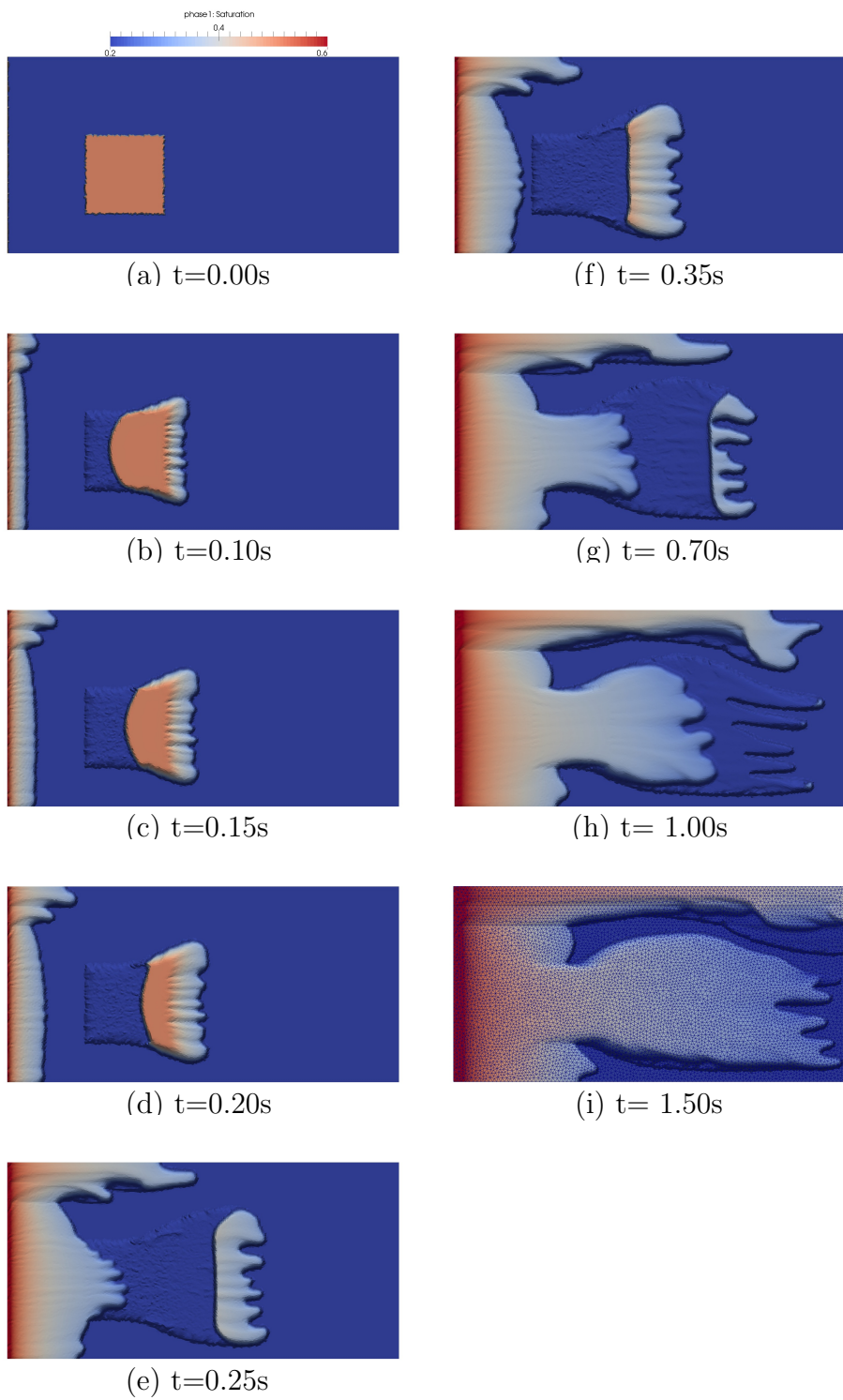


Figure 13: Impact of mesh resolution on capturing flow instabilities: snapshots of saturation field through 1.50 seconds of numerical simulation performed with fixed mesh (of 13068 elements) and  $VR=10$ . 45

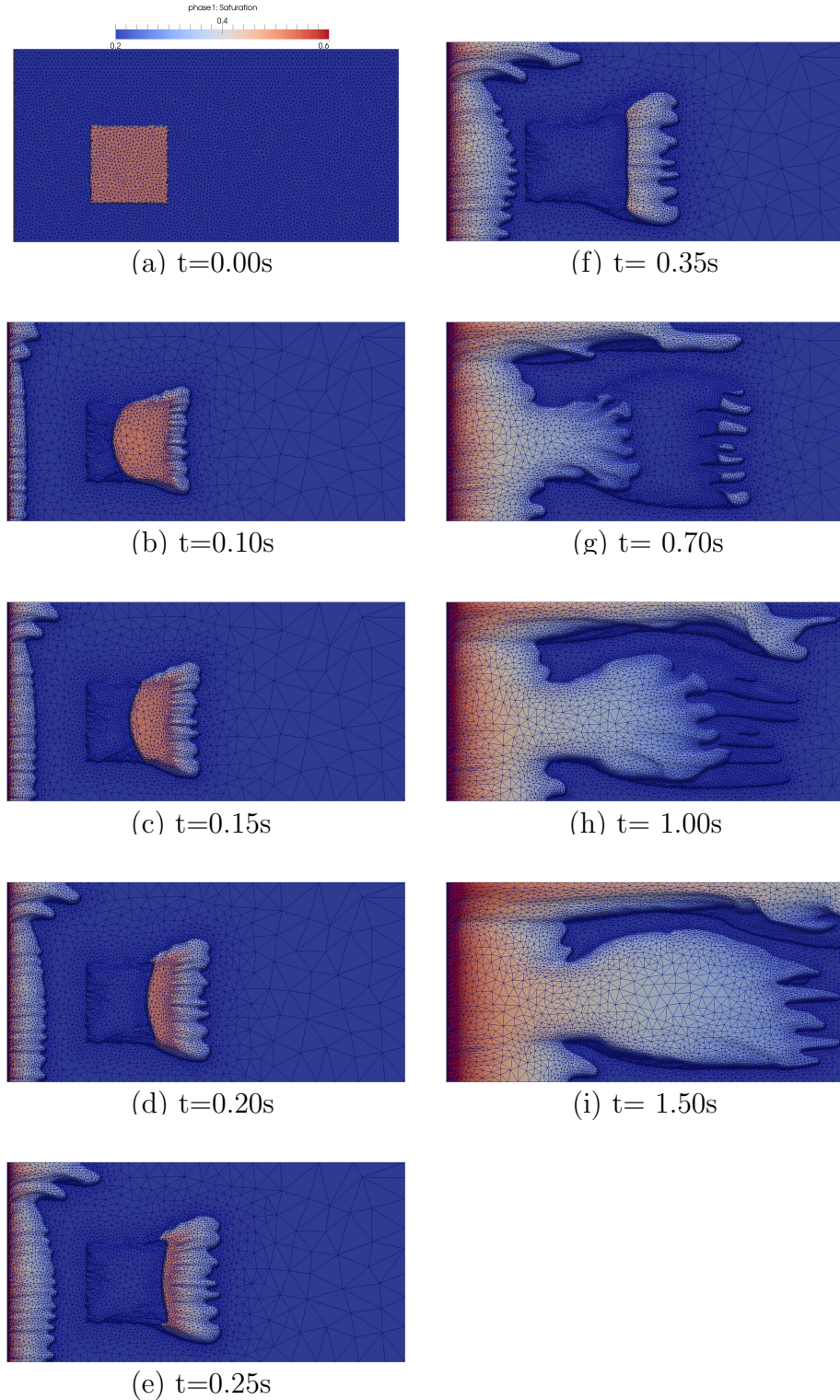


Figure 14: Impact of mesh resolution on capturing flow instabilities: snapshots of saturation field through 1.50 seconds of numerical simulation performed with adaptive mesh and  $VR=10$ .

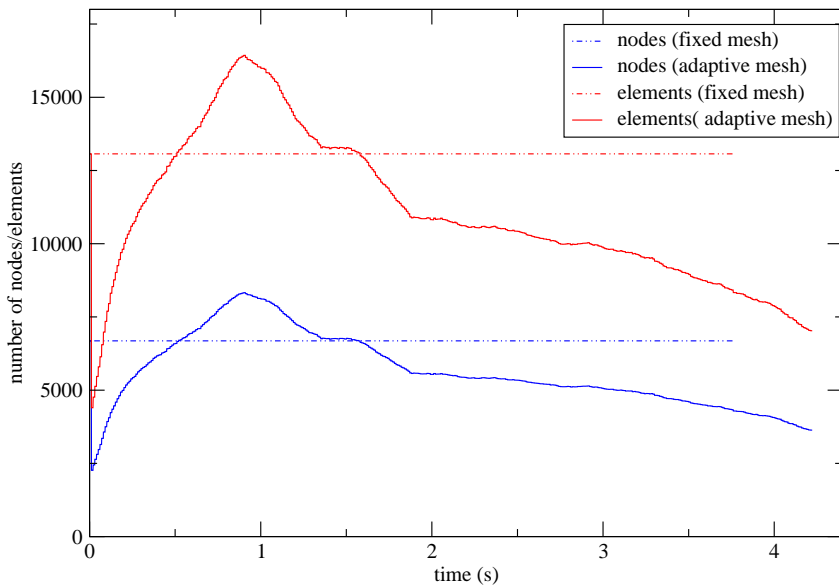
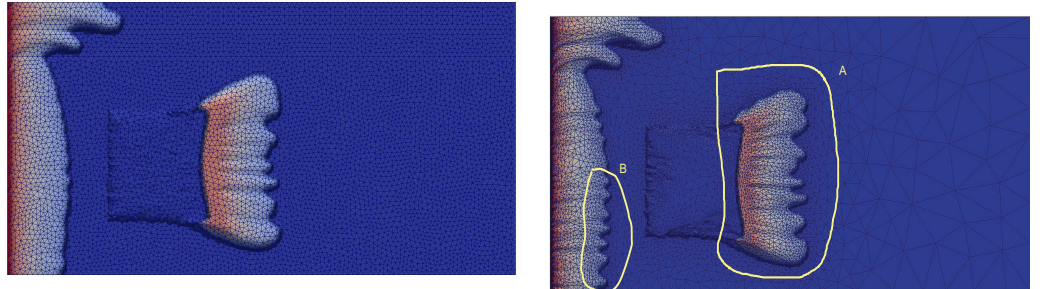
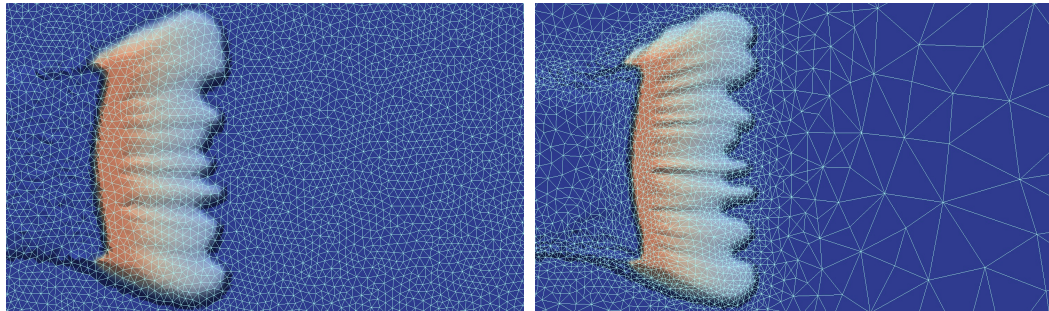


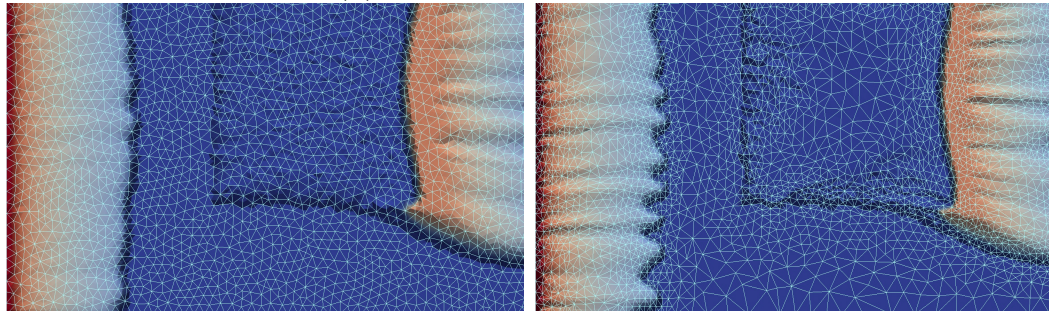
Figure 15: Impact of mesh resolution on capturing flow instabilities: total number of elements (red) and nodes (blue) for simulations performed with fixed (dotted line) and adaptive (full line) mesh.



(a) fixed and adaptive mesh



(b) Zoom on region *A*



(c) Zoom on region *B*

Figure 16: Impact of mesh resolution on flow instabilities: capturing formation and growth of flow instabilities at fluid interfaces ( $t = 0.20$  s) in two regions of the computational domain, *A* and *B*. Simulations were conducted with fixed (left-hand side) and adaptive meshes.

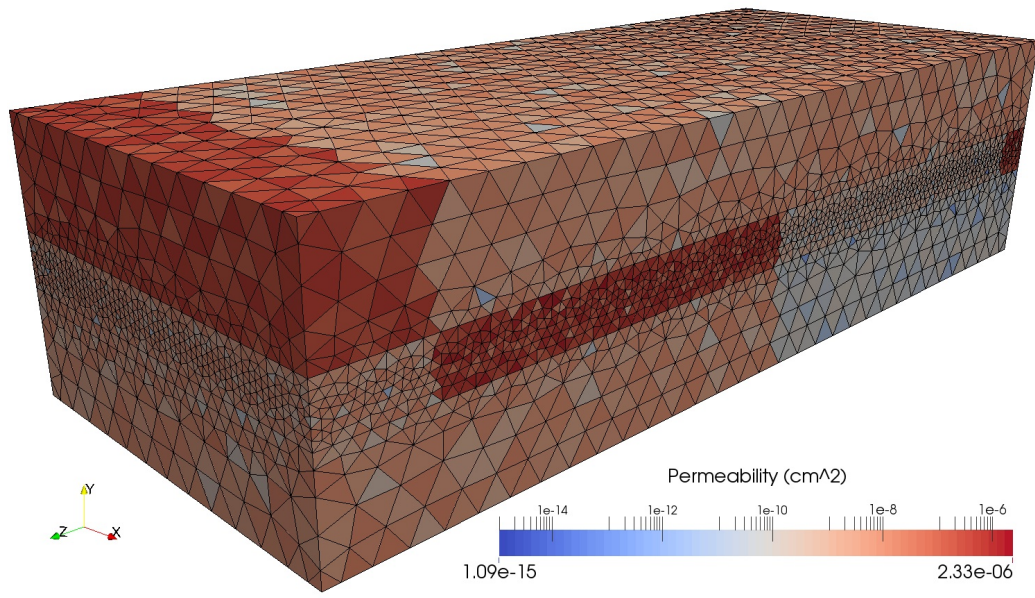


Figure 17: 3D channel flow: Permeability distribution within the computational domain, containing 235242 P<sub>1</sub>DG-P<sub>1</sub>DG element-pairs.

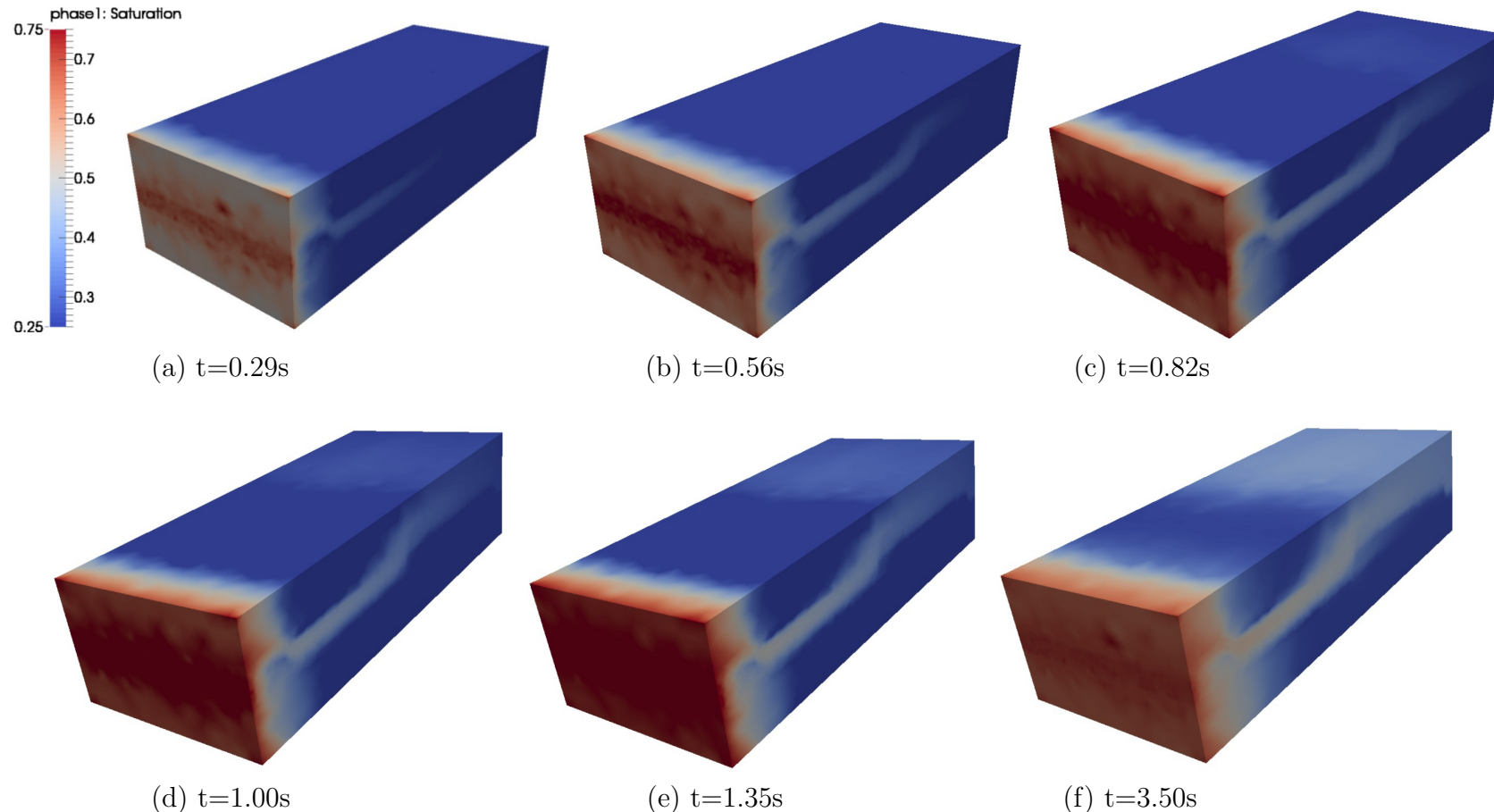


Figure 18: 3D channel flow (fixed mesh): saturation front evolving in time and space with preferential flow pathways through 3.50 seconds of numerical simulations. Preferential flow pathway can be readily noticed in these frames, mirroring permeability distribution. The domain contains 235242 P<sub>1</sub>DG-P<sub>1</sub>DG elements.

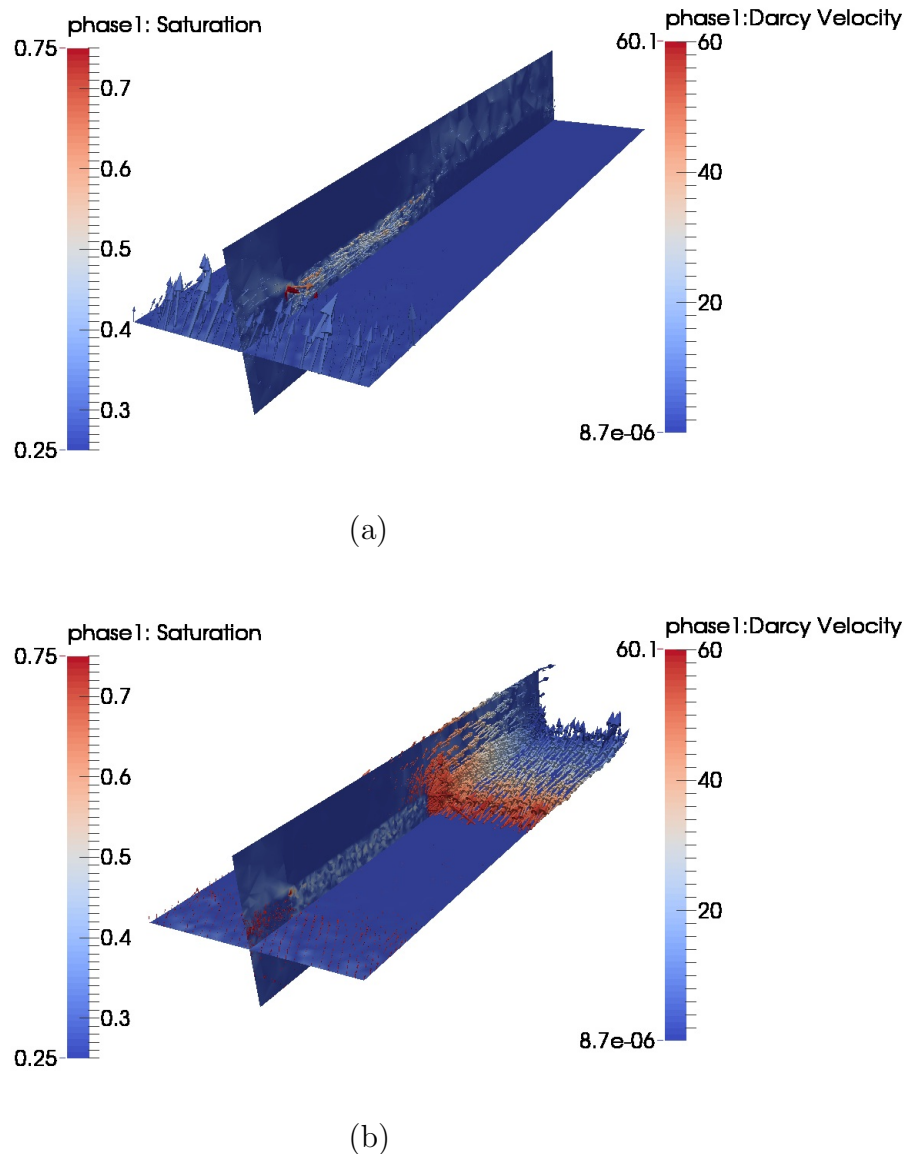


Figure 19: 3D channel flow (fixed mesh): XY and YZ planes showing wetting phase saturation overlapped with Darcy velocity vectors (in  $\text{cm} \cdot \text{s}^{-1}$ ) at (a)  $t=0.29\text{s}$  and (b)  $t=4.3\text{s}$ .

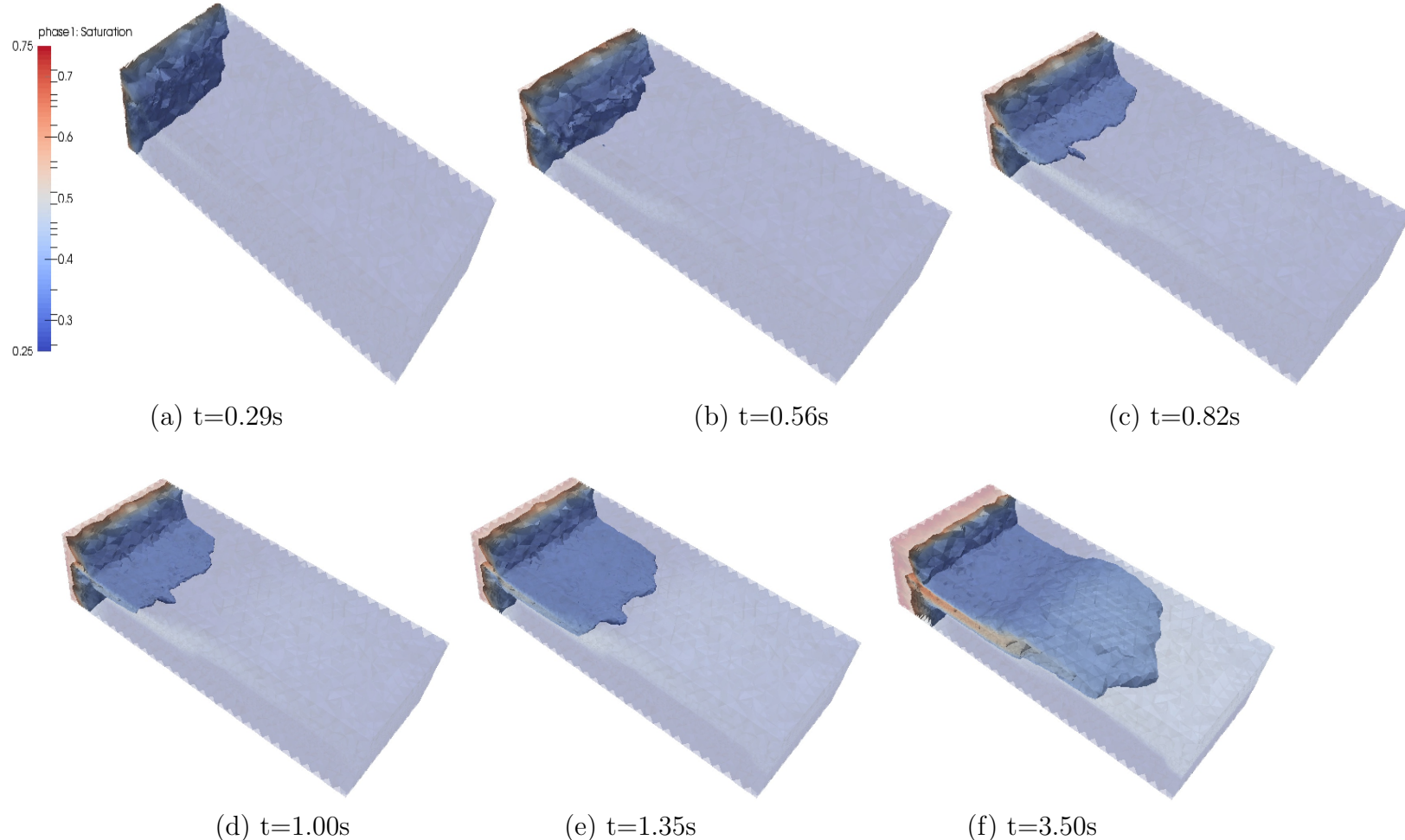


Figure 20: 3D channel flow (fixed mesh): Isosurfaces for wetted phase saturation ranging from 0.45 and 0.60 at the same instants of time of Fig. 18. Preferential flow pathway can be readily noticed in (b) and (f). Fingers' formation and growth can be clearly noticed in (b)-(e). The domain contains 235242 P<sub>1</sub>DG-P<sub>1</sub>DG elements.

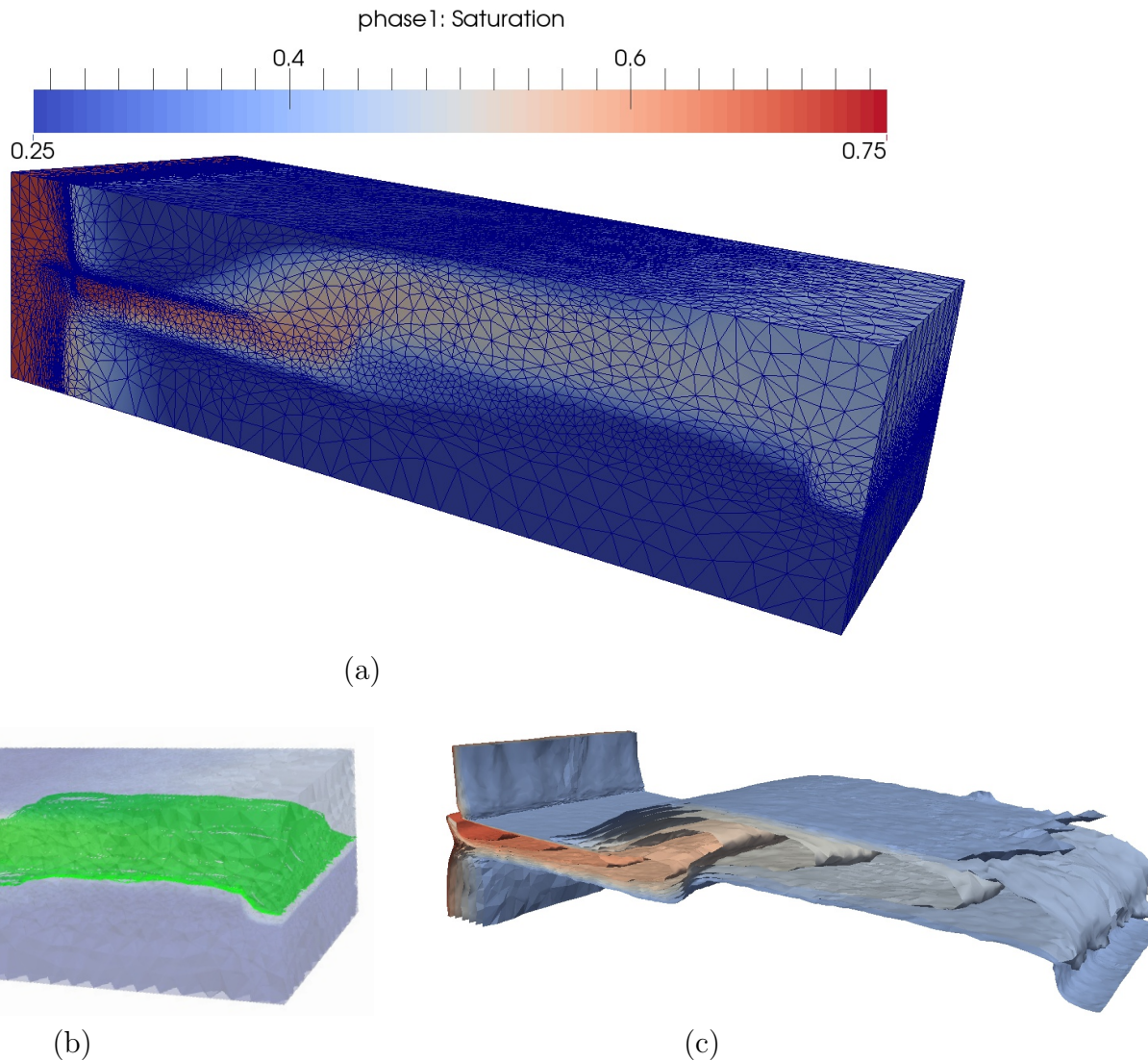


Figure 21: 3D Channel (adaptive mesh): (a) Wetting fluid saturation overlapped with mesh; (b) streamlines and; (c) isosurfaces. All plots are shown at 3.78s (Fig. 22f).

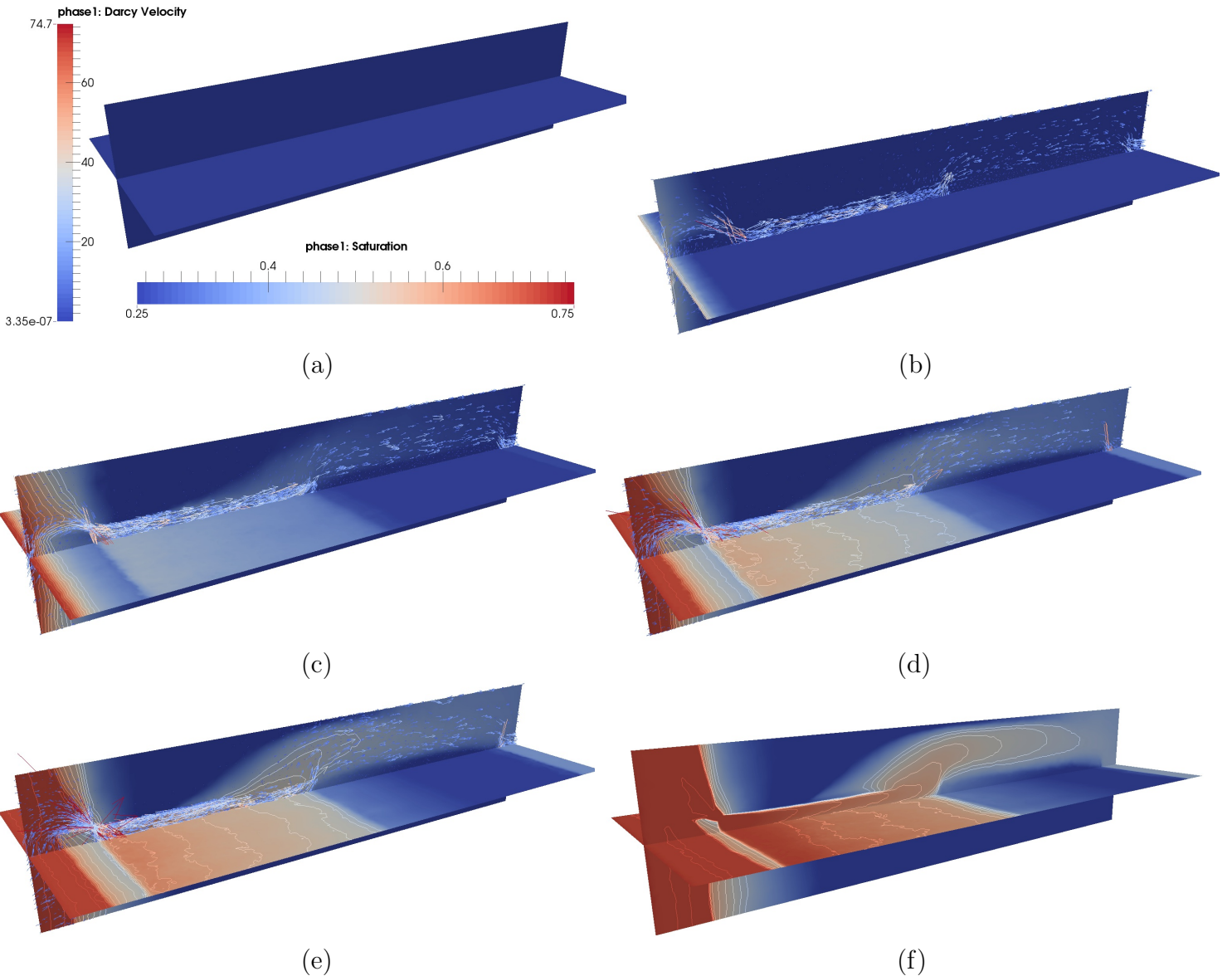


Figure 22: 3D Channel (adaptive mesh): XY and YZ planes showing wetting fluid saturation overlapped with Darcy velocity vectors at (a) 0.00, (b) 0.09, (c) 0.71, (d) 1.75, (e) 2.47 and (f) 3.78s. Colour scheme for saturation profile is the same as used in Fig. 23.

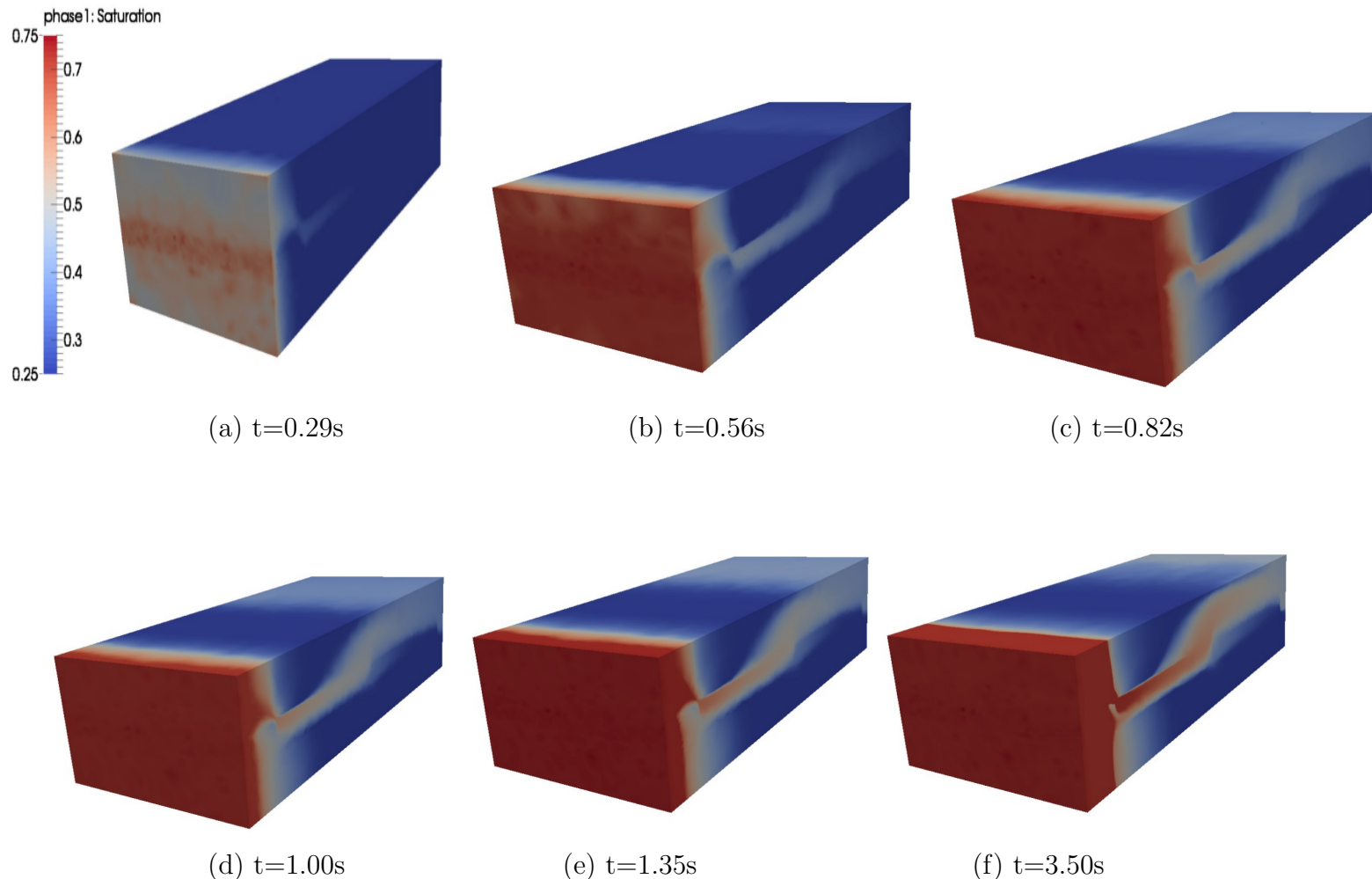


Figure 23: 3D channel flow (adaptive mesh): numerical simulation was performed with the smae boundary and initial conditions as in Figs. 17-20 with an adaptive mesh. Flow pathway is very similar to the one shown in Fig. 18.